J|A|C|S ARTICLES

Published on Web 05/11/2009

Solid-State and Solution Rearrangements of $F_3S{\equiv}NXeF^+$ Leading to the $F_4S{=}NXe^+$ Cation; Syntheses, HF Solvolyses, and Structural Characterizations of $[F_4S{=}NXe][AsF_6]$ and $[F_4S{=}NH_2][AsF_6]$

Gregory L. Smith, Hélène P. A. Mercier, and Gary J. Schrobilgen*

Department of Chemistry, McMaster University, Hamilton, Ontario L8S 4M1, Canada

Received February 15, 2009; E-mail: schrobil@mcmaster.ca

Abstract: The salt, $[F_4S{=}NXe][AsF_6]$, has been synthesized by the solid-state rearrangement of $[F_3S{\equiv}NXeF][AsF_6]$ and by HF-catalyzed rearrangement of $[F_3S{\equiv}NXeF][AsF_6]$ in anhydrous HF (aHF) and HF/BrF_5 solvents. The $F_4S{=}NXe^+$ cation undergoes HF solvolysis to form $F_4S{=}NH_2^+$, XeF_2, and the recently reported $F_5SN(H)Xe^+$ cation. Both $[F_4S{=}NXe][AsF_6]$ and $[F_4S{=}NH_2][AsF_6]$ have been characterized by ^{129}Xe and ^{19}F NMR spectroscopy in aHF and HF/BrF_5 solvents and by single-crystal X-ray diffraction. The $[F_4S{=}NXe][AsF_6]$ salt was also characterized by Raman spectroscopy. The Xe−N bond of $F_4S{=}NXe^+$ is among the shortest Xe−N bonds presently known (2.084(3) Å), and the cation interacts with the AsF_6^- anion by means of a Xe---F−As bridge in which the Xe---F distance (2.618(2) Å) is significantly less than the sum of the Xe and F van der Waals radii. Both $F_4S{=}NXe^+$ and $F_4S{=}NH_2^+$ exhibit trigonal bipyramidal geometries about sulfur, with nitrogen in the equatorial plane and the nitrogen substituents coplanar with the axial fluorine ligands of sulfur. The $F_4S{=}NH_2^+$ cation is isoelectronic with $F_4S{=}CH_2$ and, like $F_4S{=}CH_2$, has a high barrier to rotation about the S=N double bond and to pseudorotation of the trigonal bipyramidal $F_4S{=}N-$ moiety. The solution and solid-state rearrangements of $F_3S{\equiv}NXeF^+$ to $F_4S{=}NXe^+$ are proposed to result from attack at sulfur by fluoride ion arising from HF in solution and from the AsF_6^- anion in the solid state. Quantum-chemical calculations were employed to calculate the gas-phase geometries, charges, bond orders, valencies, and vibrational frequencies of $F_4S{=}NXe^+$ and $F_4S{=}NH_2^+$. The $F_4S{=}NXe^+$ cation provides the first example of xenon bonded to an imido-nitrogen, and together with the $F_4S{=}NH_2^+$ cation are presently the only cations known to contain the $F_4S{=}N$-group. Both cations are intermediates in the HF solvolysis pathways of $F_3S{\equiv}NXeF^+$ which lead to $F_5SN(H)Xe^+$ and $F_5SNH_3^+$, and significantly extend the chemistry of the $F_4S{=}N$-group.

Introduction

Several xenon(II) species are known in which xenon is bound to nitrogen having formal sp, sp^2, and sp^3 hybridization. Most belong to a weakly bonded class of XeF^+ adducts with mainly organic nitrogen bases. Those exhibiting formal nitrogen sp hybridization are represented by the XeF^+ adducts of thiazyl trifluoride,[1] hydrogen cyanide,[2,3] alkylnitriles,[2] pentafluorobenzenenitrile,[2] and perfluoroalkylnitriles.[2,4] Examples of XeF^+ adducts with sp^2-hybridized organic nitrogen bases are also known, namely, those with *s*-trifluorotriazine[4] and several perfluoropyridines.[5] The only examples in which xenon is bonded to sp^3-hybridized nitrogen are $F_5SN(H)Xe^+$ [6] and $F_5TeN(H)Xe^+$.[7] Until the present study, the only species bonded to sp^2-hybridized nitrogen atoms of inorganic ligands were those derived from the imidobis(sulfurylfluoride) group and included $FXeN(SO_2F)_2$,[8−10] $Xe[N(SO_2F)_2]_2$,[9,11] $F[XeN(SO_2F)_2]_2^+$,[9,11,12] and $XeN(SO_2F)_2^+$,[12] as well as the related imidobis(sulfuryltrifluoromethyl) group, which is solely represented by $Xe[N(SO_2CF_3)_2]_2$.[13]

Species containing the $F_4S{=}N$-group are presently limited to the neutral molecules $F_4S{=}NL$ (L = F,[14−17] CH_3,[18−21]

(1) Smith, G. L.; Mercier, H. P. A.; Schrobilgen, G. J. *Inorg. Chem.* **2007**, *46*, 1369–1378.
(2) Emara, A. A. A.; Schrobilgen, G. J. *J. Chem. Soc., Chem. Commun.* **1987**, 1644–1646.
(3) Emara, A. A. A.; Schrobilgen, G. J. *Inorg. Chem.* **1992**, *31*, 1323–1332.
(4) Schrobilgen, G. J. *J. Chem. Soc., Chem. Commun.* **1988**, 1506–1508.
(5) Emara, A. A. A.; Schrobilgen, G. J. *J. Chem. Soc., Chem. Commun.* **1988**, 257–259.
(6) Smith, G. L.; Mercier, H. P. A.; Schrobilgen, G. J. *Inorg. Chem.* **2008**, *47*, 4173–4184.
(7) Fir, B. A.; Whalen, J. M.; Mercier, H. P. A.; Dixon, D. A.; Schrobilgen, G. J. *Inorg. Chem.* **2006**, *45*, 1978–1996.
(8) LeBlond, R. D.; DesMarteau, D. D. *J. Chem. Soc., Chem. Commun.* **1974**, 555–556.
(9) DesMarteau, D. D.; LeBlond, R. D.; Hossain, S. F.; Nothe, D. *J. Am. Chem. Soc.* **1981**, *103*, 7734–7739.
(10) Sawyer, J. F.; Schrobilgen, G. J.; Sutherland, S. J. *Inorg. Chem.* **1982**, *21*, 4064–4072.
(11) Schumacher, G. A.; Schrobilgen, G. J. *Inorg. Chem.* **1983**, *22*, 2178–2183.
(12) Faggiani, R.; Kennepohl, D. K.; Lock, C. J. L.; Schrobilgen, G. J. *Inorg. Chem.* **1986**, *25*, 563–571.
(13) Foropoulos, J. J.; DesMarteau, D. D. *J. Am. Chem. Soc.* **1982**, *104*, 4260–4261.
(14) DesMarteau, D. D.; Eysel, H. H.; Oberhammer, H.; Günther, H. *Inorg. Chem.* **1982**, *21*, 1607–1616.

10.1021/ja901187n CCC: $40.75

Scheme 1. Proposed (a) Solution and (b) Solid-State Rearrangements of $F_3S{\equiv}NXeF^+$ Leading to $F_4S{=}NXe^+$

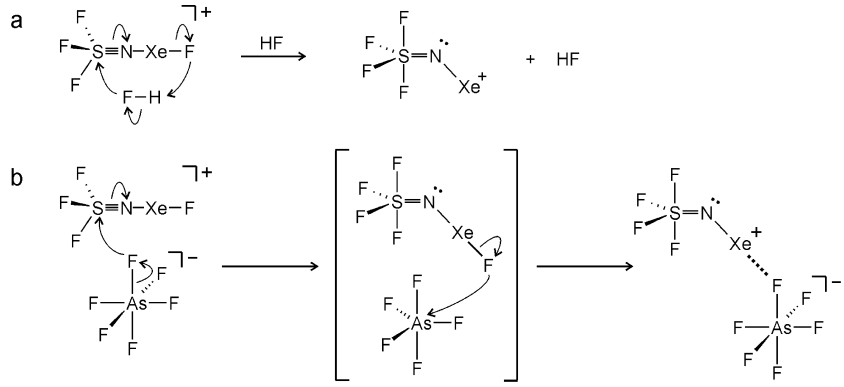

CH_2CH_3,[20] CF_3,[22−24] CF_2CF_3,[25] SF_5,[26−28] SO_2F,[29,30] and $C(O)N(CH_2CH_3)_2$[31]) and $F_4S{=}N^{\bullet}$.[32] The majority have been characterized by vibrational[14,18,20,22,25,26,29,31] and NMR[15,18−20,23−26,29,31] spectroscopy, and a number have been characterized by electron diffraction[14,19] and microwave spectroscopy.[14,19]

Solvolysis of $N{\equiv}SF_3$ in anhydrous HF (aHF) occurs by the addition of two molecules of HF across the sulfur-nitrogen triple bond to give the primary amine, F_5SNH_2,[33] whereas solvolysis of $N{\equiv}SF_3$ in the superacid medium, AsF_5/aHF, results in amine protonation to give $[F_5SNH_3][AsF_6]$.[21] Controlled solvolysis of $[F_3S{\equiv}NXeF][AsF_6]$ in aHF at −20 °C for 4 h has recently been shown to yield the $F_5SN(H)Xe^+$ and $F_5SNH_3^+$ cations,[6] but no intermediates were isolated.

In the current work, the intermediacy of $F_4S{=}NXe^+$ in the reaction pathways that lead to the $F_5SN(H)Xe^+$ and $F_4S{=}NH_2^+$ cations is documented, as well as the HF solvolyses of the $F_4S{=}NXe^+$, $F_4S{=}NH_2^+$, $F_5SN(H)Xe^+$, and $F_5SNH_3^+$ cations. The solid-state rearrangement of $[F_3S{\equiv}NXeF][AsF_6]$ to form $[F_4S{=}NXe][AsF_6]$ is also reported. The syntheses and detailed structural characterizations of the $F_4S{=}NXe^+$ and $F_4S{=}NH_2^+$ cations in the solid state and in solution significantly extend the chemistry of the $F_4S{=}N$-group, providing the only cationic derivatives of this ligand group that are presently known.

Results and Discussion

Syntheses of $[F_4S{=}NXe][AsF_6]$ and $[F_4S{=}NH_2][AsF_6]$. (a) Rearrangement of $[F_3S{\equiv}NXeF][AsF_6]$ in aHF. The $F_4S{=}NXe^+$ cation was synthesized by reaction of the previously reported $[F_3S{\equiv}NXeF][AsF_6]$ salt[1] with HF for ca. 1 h at −20 °C in aHF or HF/BrF_5 solution (eq 1).

$$F_3S{\equiv}NXeF^+ \xrightarrow[HF\ or\ BrF_5]{-20\ ^\circ C} F_4S{=}NXe^+ \qquad (1)$$

The reaction likely proceeds via the HF-catalyzed rearrangement shown in Scheme 1a. The $F_4S{=}NXe^+$ cation was shown by ^{19}F and ^{129}Xe NMR spectroscopy in both solvent media to be a major component and the intermediate leading to $F_5SN(H)Xe^+$ (see NMR Spectroscopy).

(b) Solid-State Rearrangement of $[F_3S{\equiv}NXeF][AsF_6]$. The $[F_4S{=}NXe][AsF_6]$ salt was also obtained by solid-state rearrangement of $[F_3S{\equiv}NXeF][AsF_6]$. Rearrangement occurred upon warming $[F_3S{\equiv}NXeF][AsF_6]$ to 22 °C (eq 2) and was monitored by periodically quenching the sample at −160 °C and recording the Raman spectrum at this temperature.

$$[F_3S{\equiv}NXeF][AsF_6] \xrightarrow{22\ ^\circ C} [F_4S{=}NXe][AsF_6] \qquad (2)$$

Monitoring of the most intense peaks in the Raman spectra [$F_3S{\equiv}NXeF^+$, ν(XeF) 550 cm^{-1}; $F_4S{=}NXe^+$, δ(XeNS) 178 cm^{-1}] showed that $F_4S{=}NXe^+$ formed as the only product as $F_3S{\equiv}NXeF^+$ was consumed, and that no further reaction occurred after ca. 70 min at 22 °C (see Raman Spectroscopy). The resulting bright yellow solid was also characterized by ^{19}F NMR spectroscopy at −20 °C in $N{\equiv}SF_3$ solvent.

The rationale for the rearrangement and for incomplete conversion of $F_3S{\equiv}NXeF^+$ to $F_4S{=}NXe^+$ is based upon the crystal packing of $[F_3S{\equiv}NXeF][AsF_6]$,[1] which shows that the shortest cation-anion contact (2.871(5) Å) occurs between a fluorine atom of AsF_6^- and the sulfur atom of an adjacent $F_3S{\equiv}NXeF^+$ cation. This contact is significantly shorter than the sum of the fluorine and sulfur van der Waals radii (3.27 Å).[34] In the proposed solid-state reaction mechanism (Scheme 1b), a fluorine ligand of the AsF_6^- anion coordinates to the sulfur atom of an adjacent $F_3S{\equiv}NXeF^+$ cation, which leads to fluoride ion transfer and formation of the $[F_4S{=}NXe][AsF_6]$ ion pair. As the reaction proceeds, solid-state dilution of $F_3S{\equiv}NXeF^+$ and breakdown of

(15) DesMarteau, D. D.; Seppelt, K. *Angew. Chem., Int. Ed. Engl.* **1980**, *19*, 643.
(16) O'Brien, B. A.; DesMarteau, D. D. *Inorg. Chem.* **1984**, *23*, 2188–2195.
(17) DesMarteau, D. D.; Lam, W. Y.; O'Brien, B. A.; Chang, S.-C. *J. Fluorine Chem.* **1984**, *25*, 387–394.
(18) Mews, R. *Angew. Chem., Int. Ed. Engl.* **1978**, *17*, 530.
(19) Günther, H.; Oberhammer, H.; Mews, R.; Stahl, I. *Inorg. Chem.* **1982**, *21*, 1872–1875.
(20) Bartsch, R.; Henle, H.; Meier, T.; Mews, R. *Chem. Ber.* **1988**, *121*, 451–456.
(21) Meier, T.; Hoppenheit, R.; Mews, R. *Z. Anorg. Allg. Chem.* **1993**, *619*, 1241–1246.
(22) Tullock, C. W.; Coffman, D. D.; Muetterties, E. L. *J. Am. Chem. Soc.* **1964**, *86*, 357–361.
(23) Muetterties, E. L.; Mahler, W.; Packer, K. J.; Schmutzler, R. *Inorg. Chem.* **1964**, *3*, 1298–1303.
(24) Walker, N.; Fox, W. B.; De Marco, R. A.; Moniz, W. B. *J. Mol. Spectrosc.* **1979**, *34*, 295–299.
(25) Stahl, I.; Mews, R.; Glemser, O. *Angew. Chem., Int. Ed. Engl.* **1980**, *19*, 408–409.
(26) Waterfeld, A.; Mews, R. *Angew. Chem., Int. Ed. Engl.* **1982**, *21*, 354.
(27) Waterfeld, A.; Oberhammer, H.; Mews, R. *Angew. Chem., Int. Ed. Engl.* **1982**, *21*, 355.
(28) Waterfeld, A.; Mews, R. *Chem. Ber.* **1983**, *116*, 1674–1677.
(29) Meier, T.; Mews, R. *J. Fluorine Chem.* **1989**, *42*, 81–85.
(30) Meier, T.; Mews, R. *Chem. Ber.* **1993**, *126*, 2437–2439.
(31) Clifford, A. F.; Howell, J. L. *J. Fluorine Chem.* **1977**, *10*, 431–432.
(32) Boate, A. R.; Morton, J. R.; Preston, K. F. *J. Phys. Chem.* **1976**, *80*, 409–412.
(33) Clifford, A. F.; Duncan, L. C. *Inorg. Chem.* **1966**, *5*, 692–693.
(34) Bondi, A. *J. Phys. Chem.* **1964**, *68*, 441–451.

Scheme 2. Calculated Relative Gas-Phase Energies of Products Resulting from HF-Catalyzed Rearrangement of $F_3S{\equiv}NXeF^+$ and HF Solvolysis of $F_4S{=}NXe^+$ [kJ mol^{-1}; MP2/aug-cc-pVTZ(-PP)]

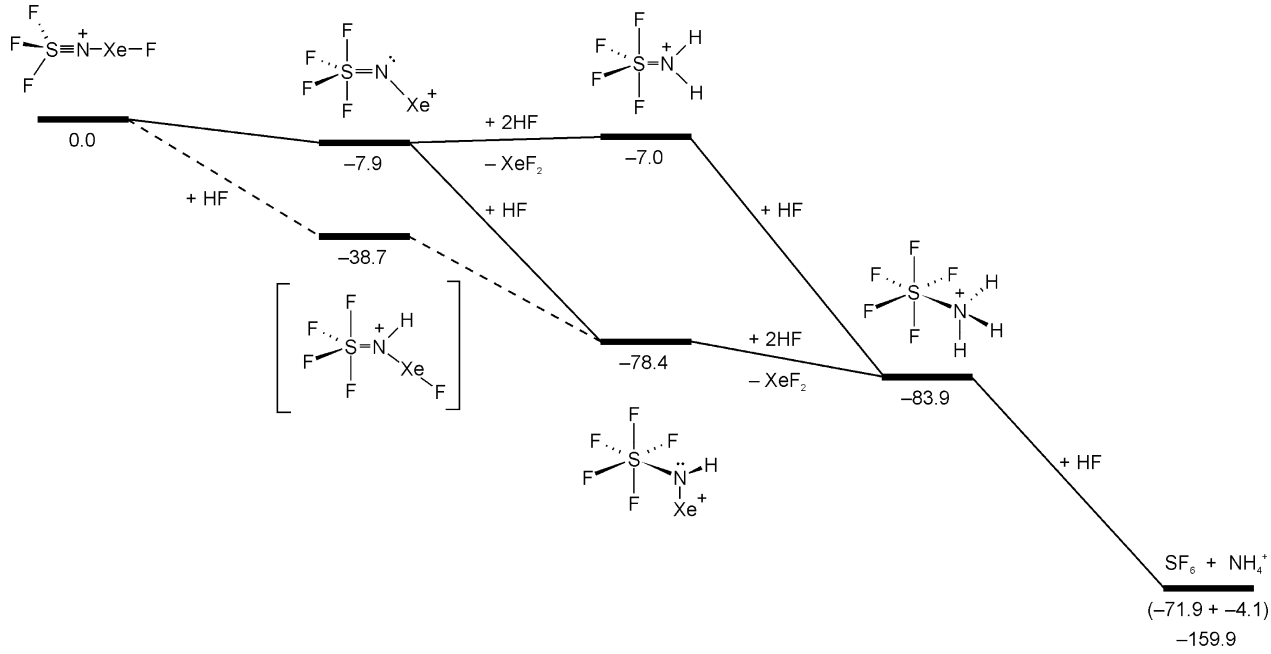

the crystal lattice disrupt fluoride ion transfer and rearrangement, preventing the rearrangement from going to completion. Determination of a yield for this reaction was not possible because $F_3S{\equiv}NXeF^+$[1] and $F_4S{=}NXe^+$ (see Raman Spectroscopy) share no directly comparable intense Raman bands. After rearrangement had ceased, the sample was stored at −78 °C for several weeks with no sign of further reaction. The proposed rearrangement pathway is also consistent with the optimized, zero-point-corrected energies of the $F_3S{\equiv}NXeF^+$ and $F_4S{=}NXe^+$ cations which show that $F_4S{=}NXe^+$ is 7.9 kJ mol^{-1} lower in energy than the $F_3S{\equiv}NXeF^+$ cation at the MP2/aug-cc-pVTZ(-PP) level of theory.

(c) Synthesis of $[F_4S{=}NH_2][AsF_6]$. The $F_4S{=}NH_2^+$ cation was formed concurrently with $F_4S{=}NXe^+$ during the solvolysis of $F_3S{\equiv}NXeF^+$ in aHF at −20 °C. Reaction of $F_4S{=}NXe^+$ with 2 equiv of HF resulted in $F_4S{=}NH_2^+$ and XeF_2 formation according to eq 3, which were identified by ^{19}F NMR spectroscopy (vide infra).

$$[F_4S{=}NXe][AsF_6] + 2HF \xrightarrow[HF\ or\ BrF_5]{-20\ °C} [F_4S{=}NH_2][AsF_6] + XeF_2 \quad (3)$$

Characterization by Raman spectroscopy was not attempted because it was not possible to isolate $[F_4S{=}NH_2][AsF_6]$ as a pure product from the complex admixture of solvolysis products comprised of $[F_4S{=}NXe][AsF_6]$, $[F_5SN(H)Xe][AsF_6]$, $[F_5SNH_3][AsF_6]$, $[NH_4][AsF_6]$, SF_6, and XeF_2.

(d) Solvolytic Pathways and Thermodynamic Considerations. It has recently been shown that HF solvolysis of $F_3S{\equiv}NXeF^+$ led to the formation of the $F_5SN(H)Xe^+$ and $F_5SNH_3^+$ cations.[6] The identification and characterization of $F_4S{=}NXe^+$ and $F_4S{=}NH_2^+$ as intermediates in the present study provide a fuller understanding of the reaction pathways that lead to the aforementioned cations. Proposed reaction pathways that account for the products, along with their relative energies, are provided in Scheme 2.

The solvolysis of the $F_3S{\equiv}NXeF^+$ cation is likely initiated by HF-catalyzed rearrangement to $F_4S{=}NXe^+$ (Scheme 1a), which occurred at a much lower temperature (−20 °C) in HF or HF/BrF_5 solution than the fluoride ion-catalyzed solid-state rearrangement (22 °C, Scheme 1b). Moreover, $F_3S{\equiv}NXeF^+$ did not undergo rearrangement in BrF_5 solvent at −20 °C in the absence of HF.

Two pathways for the solvolysis of $F_4S{=}NXe^+$ are possible: (1) reaction with 2 equiv of HF to form $F_4S{=}NH_2^+$ and XeF_2 (eq 3), and (2) addition of HF across the S=N double bond of $F_4S{=}NXe^+$ to give $F_5SN(H)Xe^+$ (eq 4).

$$[F_4S{=}NXe][AsF_6] + HF \xrightarrow[HF\ or\ BrF_5]{-20\ °C} [F_5SN(H)Xe][AsF_6] \quad (4)$$

Both cations may undergo further HF attack by (1) reaction of $F_5SN(H)Xe^+$ with 2 equiv of HF to form the very stable $F_5SNH_3^+$ cation and XeF_2 according to equilibrium 5,[6] and/or (2) addition of HF across the S=N double bond of $F_4S{=}NH_2^+$ to form $F_5SNH_3^+$ (eq 6).

$$[F_5SN(H)Xe][AsF_6] + 2HF \rightleftharpoons [F_5SNH_3][AsF_6] + XeF_2 \quad (5)$$

$$[F_4S{=}NH_2][AsF_6] + HF \xrightarrow[HF\ or\ BrF_5]{>0\ °C} [F_5SNH_3][AsF_6] \quad (6)$$

Fluorine-19 NMR spectroscopy showed that the $F_5SN(H)Xe^+$ cation was initially formed, along with $F_4S{=}NXe^+$ and $F_4S{=}NH_2^+$, at −20 °C. Initial formation of $F_5SN(H)Xe^+$ may arise from HF addition across the $F_3S{\equiv}NXeF^+$ triple bond to form $F_4S{=}N(H)XeF^+$ as an intermediate which subsequently undergoes rearrangement to form the known $F_5SN(H)Xe^+$ cation[6] (Scheme 2). Although the $F_4S{=}N(H)XeF^+$ cation is thermodynamically favorable, it was not observed experimentally. When the reaction mixture was warmed to 0 °C, $F_5SNH_3^+$ formation was favored while $F_4S{=}NXe^+$ was consumed and $F_4S{=}NH_2^+$ remained. Above 0 °C, the $F_5SNH_3^+$ cation dominated (eqs 5 and 6), along with increasing amounts of its solvolysis products, SF_6 and NH_4^+, and a trace amount of F_5SNF_2, which was presumably generated by a series of reactions that are analogous to those described for $F_5SN(H)Xe^+$ [6] and $F_5TeN(H)Xe^+$.[7] With careful temperature control, it was possible to record the ^{19}F NMR spectrum of the entire

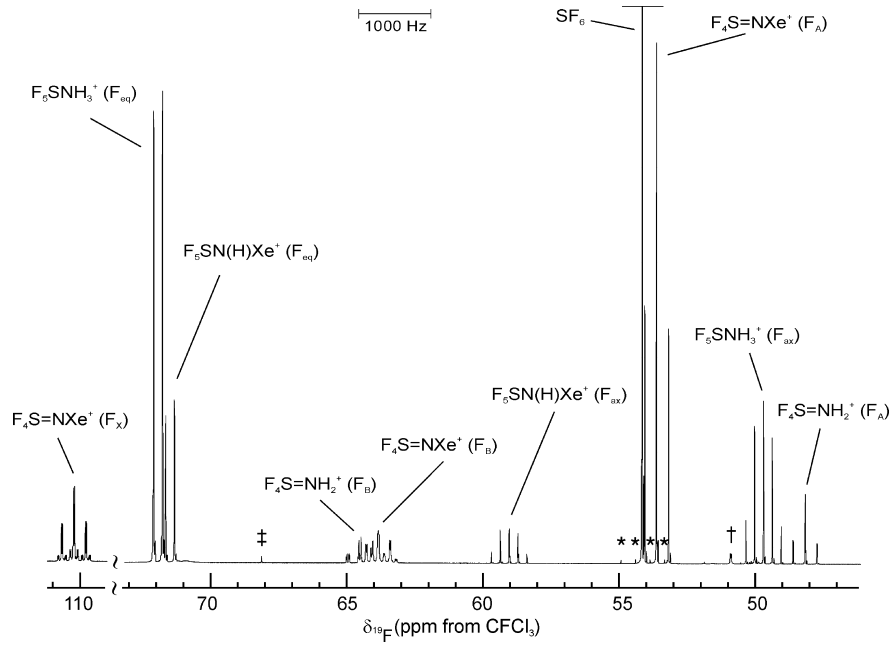

Figure 1. Fluorine-19 NMR spectrum (470.592 MHz) of a product mixture resulting from the solvolysis of $[F_3S{\equiv}NXeF][AsF_6]$ for 30 min in aHF solvent at −20 °C; symbols denote F-on-S of residual $F_3S{\equiv}NXeF^+$ (†), the 1:1:1:1 quartet arising from $^1J(^{19}F{-}^{33}S)$ of SF_6 (*), and a very weak unassigned resonance at 68.1 ppm (‡). The XeF_2 resonance, not shown in the spectral trace, occurred at $\delta(^{19}F) = -194.5$ ppm with $^1J(^{19}F{-}^{129}Xe) = 5652$ Hz.

Table 1. ^{19}F and ^{129}Xe NMR Parameters for $[F_4S{=}NXe][AsF_6]$ and $[F_4S{=}NH_2][AsF_6]$[a]

	chemical shifts, ppm				coupling constants, Hz					
cations	$\delta(^{129}Xe)$	$\delta(^{19}F_A)$	$\delta(^{19}F_B)$	$\delta(^{19}F_X)$	$^2J(^{19}F_A{-}^{19}F_B)$	$^2J(^{19}F_A{-}^{19}F_X)$	$^2J(^{19}F_B{-}^{19}F_X)$	$^3J(^{129}Xe{-}^{19}F_B)$	$^3J(^{129}Xe{-}^{19}F_X)$	$^3J(^{19}F_B{-}^{1}H)_{syn}$
$F_4S{=}NXe^+$ [b]	−2674	53.6	63.8	110.2	206.8	206.5	18.2	203.6	129.7	
	(−2588)	(55.1)	(64.7)	(113.3)	(212.3)	(210.2)	(18.0)	(208.7)	(126.7)	
	[−2510]	[58.6]	[c]	[110.6]	[206.3]	[209.6]	[21.6]	[208.9]	[102.0]	
$F_4S{=}NH_2^+$ [d]		48.1	64.5		205.4					42.5
		(49.6)	(66.5)		(203.5)					(38.2)

[a] The values in parentheses were measured in HF/BrF_5 solvent at −60 °C, and the values in square brackets were measured in $N{\equiv}SF_3$ solvent at 0 °C; all other values were measured in HF solvent at −20 °C. The AsF_6^- anion resonance in HF solvent was broad (saddle-shaped) [$\delta(^{19}F) = -69$ (−64) ppm, $\Delta\nu_{1/2} = 2860$ (700) Hz] and results from a partially quadrupole-collapsed 1:1:1:1 quartet arising from $^1J(^{75}As{-}^{19}F)$. The NMR parameters for HF solvent are $\delta(^{19}F) = -197$ (−192) ppm, $\delta(^1H) = 8.26$ (7.39) ppm, and those for BrF_5 solvent are $\delta(^{19}F_{eq}) = 134.5$ ppm, $\delta(^{19}F_{ax}) = 272.0$ ppm, $^2J(^{19}F_{ax}{-}^{19}F_{eq}) = 76.3$ Hz. [b] The fluorine atom labeling scheme is given by structure I. One-bond secondary isotope effects were observed for $F_4S{=}NXe^+$ in HF solvent; $^1\Delta^{19}F_A(^{34/32}S) = -0.064$ ppm, $^1\Delta^{19}F_B(^{34/32}S) = -0.055$ ppm, and $^1\Delta^{19}F_X(^{34/32}S) = -0.055$ ppm. All coupling constants have positive signs based on the spectral simulations. The $^3J(^{129}Xe{-}^{19}F_A)$ coupling constant of $F_4S{=}NXe^+$ was too small to be resolved in all solvents. [c] The $^{19}F_B$ resonance in $N{\equiv}SF_3$ solvent was not observed because of overlap with the solvent. [d] The fluorine atom labeling scheme is given by structure II. Additional coupling constants obtained from spectral simulations are $^3J(^{19}F_B{-}^1H)_{anti} = -1.1$ Hz, $^3J(^{19}F_A{-}^1H) = -3.6$ Hz, $^2J(^1H{-}^1H) = 14.9$ Hz. Secondary isotope effects were observed for $F_4S{=}NH_2^+$ in HF solvent; $^1\Delta^{19}F_A(^{34/32}S) = -0.061$ ppm and $^1\Delta^{19}F_B(^{34/32}S) = -0.049$ ppm.

$F_3S{\equiv}NXeF^+$ solvolysis product mixture with the exception of F_5SNF_2 (Figure 1).

NMR Spectroscopy. The ^{19}F and ^{129}Xe NMR parameters for the AsF_6^- salt of the $F_4S{=}NXe^+$ cation (structure I), recorded in aHF, BrF_5 containing a catalytic amount of HF (hereafter designated HF/BrF_5), and $N{\equiv}SF_3$ solvents, and the ^{19}F NMR parameters for the AsF_6^- salt of the $F_4S{=}NH_2^+$ cation (structure II), recorded in aHF and HF/BrF_5 solvents, are listed in Table

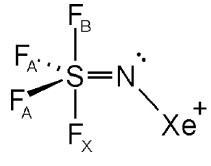

I

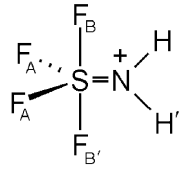

II

1. Only the ^{19}F and ^{129}Xe NMR spectra recorded in aHF at −20 °C (Figures 2−4) and their parameters are discussed in detail in this section. The ^{19}F chemical shifts and coupling constants are similar to those of $F_4S{=}NF$,[14,15] $F_4S{=}NCH_3$,[19,20] and $F_4S{=}NCF_3$.[23] Spectral assignments were confirmed by use of the program ISOTOPOMER,[35] which provided simulated spectra for the $F_4S{=}NXe^+$ and $F_4S{=}NH_2^+$ cations that are in excellent agreement with their experimental ^{19}F (Figures 3 and 4) and ^{129}Xe (Figure 2) NMR spectra. As in the cases of $F_5SN(H)Xe^+$ and $F_5SNH_3^+$,[6] the ^{14}N resonances of $F_4S{=}NXe^+$ and $F_4S{=}NH_2^+$ were not observed, presumably because quadrupolar relaxation of ^{14}N (^{14}N, $I = 1$), resulting from the high electric field gradients at the ^{14}N nuclei that result from the low symmetries around nitrogen in these cations, resulted in broad ^{14}N resonances that could not be differentiated from the spectral baselines.

(a) $[F_4S{=}NXe][AsF_6]$. The ^{19}F NMR spectrum of the $F_4S{=}NXe^+$ cation (Figure 3) is a superimposition of an A_2BX spin-coupling pattern (chemical shifts 53.6 (A_2), 63.8 (B), and

(35) Santry, D. P.; Mercier, H. P. A.; Schrobilgen, G. J. *ISOTOPOMER, A Multi-NMR Simulation Program*, version 3.02NTF; Snowbird Software, Inc.: Hamilton, ON, 2000.

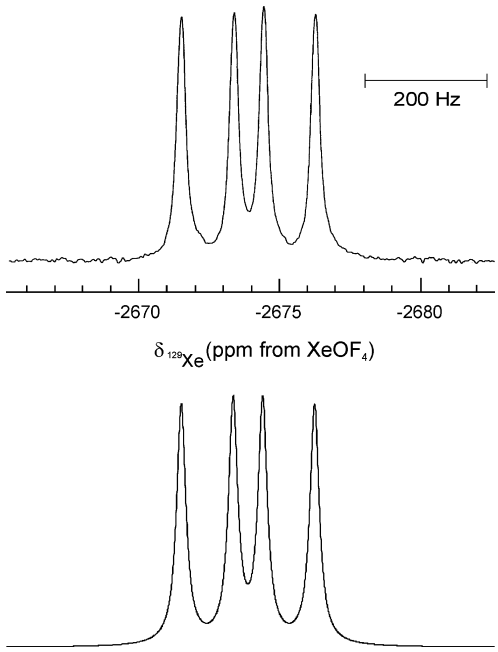

Figure 2. ^{129}Xe NMR spectrum (138.086 MHz) of $F_4S{=}NXe^+$ in HF solvent at −20 °C (upper trace) and simulated spectrum (lower trace).

110.2 (X) ppm) that arises from the $F_4S{=}N$-group (C_s symmetry) and satellite spectra arising from an $A_2BX\Omega$ spin system that results from coupling to natural abundance ^{129}Xe (26.44%, denoted by Ω). Xenon-129 satellites are only observed on the axial B and X fluorine resonances. The ^{19}F chemical shifts of the F_4S-group of $F_4S{=}NXe^+$ have chemical shift ranges and trends similar to those of $F_4S{=}NCF_2CF_3$ (66.7, 77.2, and 98.5 ppm, respectively),[25] whereas in the case of $F_4S{=}NCH_3$ (68.2, 73.9, and 76.3 ppm, respectively),[20] the trend is maintained but F_X is significantly more shielded. The chemical shift trend of the F_4S-group is, however, reversed for $F_4S{=}NF$ (52.7, 45.0, and 13.2 ppm, respectively).[14] The pseudotriplet corresponding to the equatorial F_A environment of $F_4S{=}NXe^+$ arises from a doublet of doublets that results from the two nearly equal couplings, $^2J(^{19}F_A{-}^{19}F_B) = 206.8$ Hz and $^2J(^{19}F_A{-}^{19}F_X) = 206.5$ Hz, which are similar to those of related species, e.g., $F_4S{=}NF$ (213.9 and 194.0 Hz),[14] $F_4S{=}NCH_3$ (201 and 194.0 Hz),[20] and $F_4S{=}NCF_2CF_3$ (208.0 and 210.6 Hz).[25] The F_B and F_X multiplets are each comprised of a doublet of triplets, with the triplet arising from $^2J(^{19}F_A{-}^{19}F_{B/X})$ (vide supra) and the doublets arising from $^2J(^{19}F_B{-}^{19}F_X) = 18.2$ Hz. The multiplets are accompanied by natural abundance ^{129}Xe satellites resulting from $^3J(^{129}Xe{-}^{19}F_B) = 203.6$ Hz and $^3J(^{129}Xe{-}^{19}F_X) = 129.7$ Hz, respectively, with the satellites of the central peak of the F_B multiplet overlapping with the inner satellites of the outer multiplet lines. In $N{\equiv}SF_3$ solvent, the F_B multiplet could not be observed because it overlapped with the solvent peak; however, the $^3J(^{129}Xe{-}^{19}F_B)$ coupling that is reported for this solvent was obtained from the ^{129}Xe spectrum (vide infra). The additional fine structure that is manifested in the small unequal doublet splittings on each of the F_A triplet transitions, the additional transitions in the central peak of the F_B multiplet, and the broadenings of the F_B and, to a lesser degree, the F_X resonances are due to second-order effects which were confirmed by spectral simulation. Quadrupolar relaxation resulting from ^{14}N and partially quadrupole collapsed $^{19}F{-}^{14}N$ coupling are not significant contributors to the ^{19}F line widths because the simulated ^{19}F spectra account for the spectral line widths without invoking quadrupolar relaxation and/or $^{19}F{-}^{14}N$ coupling.

The ^{129}Xe NMR spectrum of $F_4S{=}NXe^+$ (Figure 2) consists of a doublet of doublets, resulting from $^3J(^{129}Xe{-}^{19}F_B)$ and $^3J(^{129}Xe{-}^{19}F_X)$ (vide supra), centered at −2674 ppm. No $^3J(^{129}Xe{-}^{19}F_A)$ coupling could be resolved (vide infra). Failure to observe $^1J(^{129}Xe{-}^{14}N)$ likely results from the low symmetry and associated significant electric field gradient at nitrogen that results in quadrupolar relaxation and collapse of this coupling. The ^{129}Xe NMR chemical shift is consistent with that expected for xenon bound to an sp^2-hybridized nitrogen atom but is considerably more shielded than the ^{129}Xe resonances of $Xe[N(SO_2CF_3)_2]_2$ (−2444 ppm in SO_2ClF at 8 °C),[11] $Xe[N(SO_2F)_2]_2$ (−2257 ppm in SO_2ClF at −40 °C),[11] $FXeN(SO_2F)_2$ (−2009 ppm in SO_2ClF at −40 °C),[11] $XeN(SO_2F)_2^+$ (−1943 ppm in SbF_5 at 25 °C),[12] and $F[XeN(SO_2F)_2]_2^+$ (−1933 ppm in BrF_5 at −5 °C).[9] The relatively high ^{129}Xe shielding of $F_4S{=}NXe^+$ is consistent with a Xe−N bond that is significantly more covalent than those of the aforementioned species[36] (also see Computational Results), with a ^{129}Xe chemical shift that is most similar to those of xenon bound to sp^3-hybridized nitrogen in $F_5SN(H)Xe^+$ (−2897 ppm in HF at −20 °C)[6] and $F_5TeN(H)Xe^+$ (−2841 ppm in HF at −45 °C).[7] It has been shown that the ^{129}Xe shielding may be correlated with the L-group electronegativity and Xe−E bond covalency, where L is an electronegative ligand group and E is a second-row ligand atom.[6,7] Accordingly, xenon shielding generally increases with increasing Xe−E bond covalency for the series of LXe^+ cations, i.e., Xe−F < Xe−O < Xe−N < Xe−C. It is noteworthy that the $^3J(^{129}Xe{-}^{19}F_X)$ coupling in $N{\equiv}SF_3$ solvent (102.0 Hz) is significantly less than that in aHF or BrF_5 solvent (129.7 and 126.7 Hz, respectively), whereas the remaining coupling constants are very similar irrespective of solvent. This is likely a consequence of coordination of $N{\equiv}SF_3$ to the xenon atom of the cation.

The $^3J(^{19}F_A{-}^{129}Xe)$ coupling could not be resolved in either the ^{19}F or the ^{129}Xe NMR spectrum when recorded in aHF, BrF_5, or $N{\equiv}SF_3$ solvents. The small absolute to near-zero value of $^3J(^{19}F_A{-}^{129}Xe)$ may stem from a Karplus-type dependence,[37] where the absolute three-bond coupling constant is a minimum when the dihedral angle between the planes occupied by the coupled nuclei is 90°. In the present instance, the minimum is achieved when $F_A{-}S{-}N{-}Xe$ is 90°. This finding is also consistent with $F_4S{=}NF$, for which the $^3J(^{19}F_N{-}^{19}F_A)$ coupling (F_N is F-on-N) is an order of magnitude smaller than $^3J(^{19}F_N{-}^{19}F_B)$ or $^3J(^{19}F_N{-}^{19}F_X)$.[15] In the structurally related compound, $F_4P^VN(H)P^{III}F_2$,[38] the coupling constants between P(III) and the *cis*- and *trans*-axial fluorines are 209.2 and 14.7 Hz, respectively, and are of opposite sign, whereas the coupling between P(III) and the equatorial fluorines was not resolved (<0.2 Hz). The $F_A{-}P^V{-}N{-}P^{III}$ dihedral angle is expected to be 90°; however, this aspect of the structure has not been confirmed.

(b) $[F_4S{=}NH_2][AsF_6]$. The ^{19}F NMR spectrum of $F_4S{=}NH_2^+$ (Figure 4) is an $A_2BB'XX'$ spin pattern with ^{19}F NMR parameters that are in a range similar to those of isoelectronic $F_4S{=}CH_2$[39] but have chemical shifts that exhibit the opposite trend (NMR parameters for neat $F_4S{=}CH_2$ at −150 °C appear

(36) Gerken, M.; Schrobilgen, G. J. *Coord. Chem. Rev.* **2000**, *197*, 335–395.
(37) Karplus, M. *J. Chem. Phys.* **1959**, *30*, 11–15.
(38) Rankin, D. W. H.; Wright, J. G. *J. Chem. Soc., Dalton Trans.* **1979**, *6*, 1070–1074.

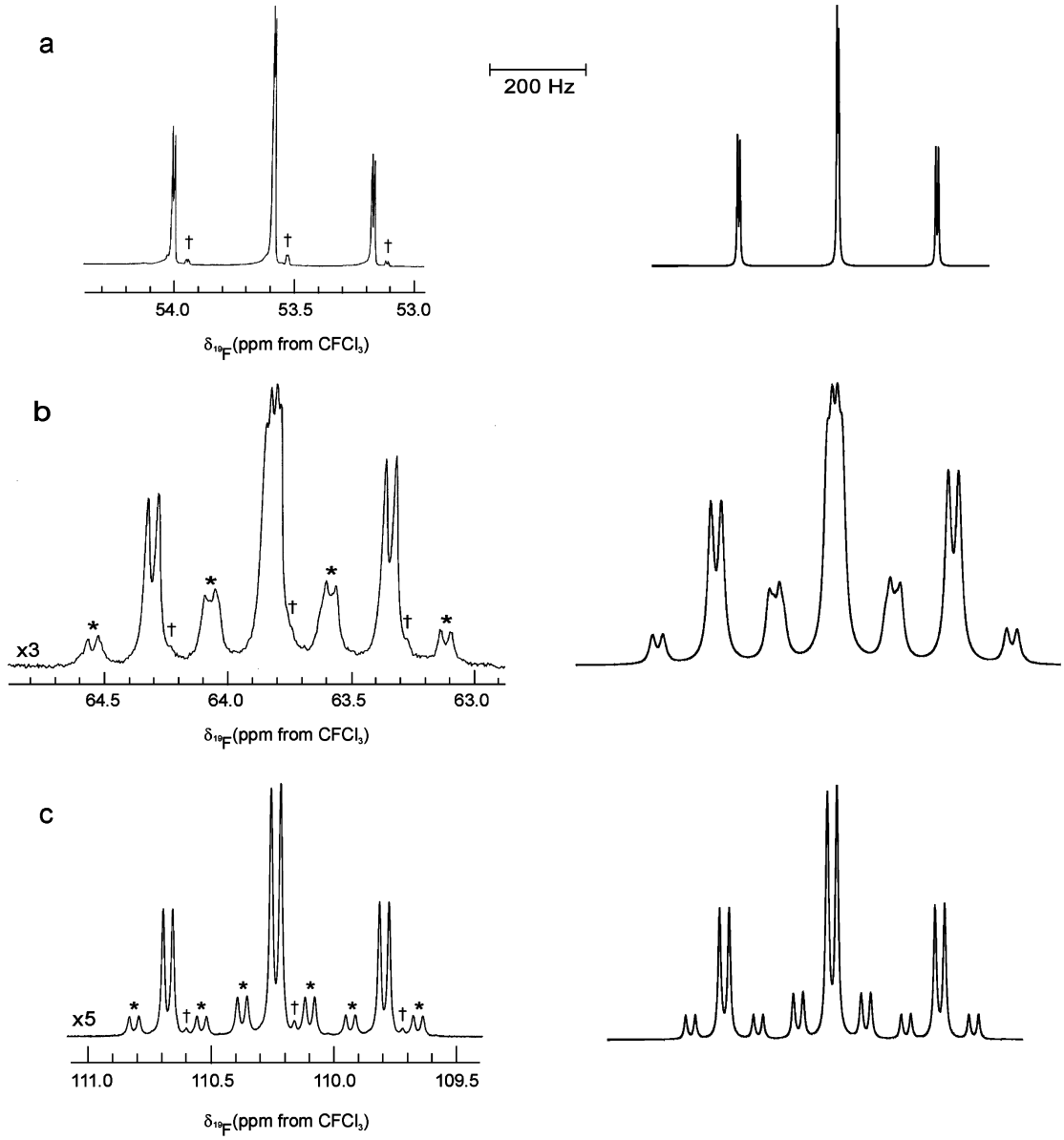

Figure 3. ^{19}F NMR spectrum (470.592 MHz) of $F_4S{=}NXe^+$ in HF solvent at −20 °C (left-hand traces) and simulated spectrum (right-hand traces) depicting (a) F_A, (b) F_B, and (c) F_X; symbols denote the $^1\Delta^{19}F(^{34/32}S)$ secondary isotope shifts (†) and ^{129}Xe satellites (*) in the experimental spectrum.

in square brackets in the ensuing discussion). Chemical shifts at 48.1 [59.0] (A_2) and 64.5 [53.6] (BB′) ppm arise from the $F_4S{=}N$-group (local C_{2v} symmetry), with additional fine structure on F_B arising from the protons (XX′) bonded to nitrogen. As previously observed for $F_4S{=}CH_2$[39] and other C-substituted derivatives, $F_4S{=}CHR$,[40] two coupling paths between the F_B and H nuclei result from the high barrier to rotation about the S=N double bond.[41] Unfortunately, the ^1H NMR spectrum of the $F_4S{=}NH_2^+$ cation was almost entirely obscured by overlap with the broad HF doublet (HF/BrF_5 solvent; −70 °C; $\delta(^1H)$, 7.44 ppm; $^1J(^1H{-}^{19}F) = 470$ Hz; $\Delta\nu_{1/2} = 700$ Hz). Only two weak transitions that may be attributable to $F_4S{=}NH_2^+$ were observed that appeared as shoulders to high frequency of the high-frequency branch of the HF doublet (8.32 and 8.72 ppm), which may be compared with the chemical shift of $F_5SNH_3^+$ (7.74 ppm)[6] under the same experimental conditions. The ^{19}F spectral features arising from two $^{19}F{-}^1H$ coupling pathways were also apparent in the ^{19}F NMR spectrum and were confirmed by simulation (Figure 4). The F_A and F_B multiplets in the ^{19}F spectrum consist of triplets that arise from $^2J(^{19}F_A{-}^{19}F_B) = 205.5$ [154.4] Hz, with the F_A resonance being further split by $^3J(^{19}F_A{-}^1H) = -3.6$ [10.5] Hz and the F_B resonance being further split by coupling with the *syn*- and *anti*-hydrogen environments, i.e., $^3J(^{19}F_B{-}^1H)_{syn} = 42.5$ [58.1] Hz and $^3J(^{19}F_B{-}^1H)_{anti} = -1.1$ [9.7] Hz. Both resonances are also influenced by $^2J(^1H{-}^1H) = 14.9$ Hz. A minor feature not reproduced by spectral simulation is the asymmetry of the outer transitions of the F_B multiplet. In the experimental spectrum, eight transitions of the high-frequency branch of the multiplet

(39) Kleemann, G.; Seppelt, K. *Angew. Chem., Int. Ed. Engl.* **1978**, *17*, 516–518.
(40) Seppelt, K. In *Synthetic Fluorine Chemistry*; Olah, G. A., Chambers, R. D., Prakash, G. K. S., Eds.; John Wiley & Sons, Inc.: Toronto, 1992; pp 87−96.
(41) Although the ^{19}F chemical shifts are comparable to those of the $F_4S{-}N(CH_3)_2^+$ cation (63.8 and 61.6 ppm, SO_2, −55 °C) [Meier, T. Mews, R. *Angew. Chem., Int. Ed. Engl.* **1985**, *24*, 344–345], the low-temperature NMR study shows no evidence for hindered rotation about the S−N bond, ruling out the iminium valence isomer, $F_4S{=}N(CH_3)_2^+$.

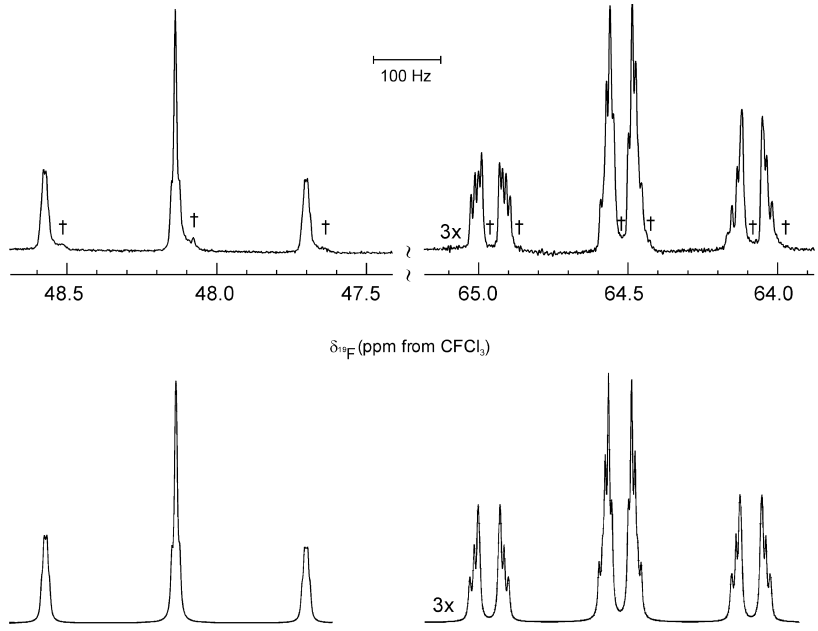

Figure 4. Experimental ^{19}F NMR spectrum (470.592 MHz) of $F_4S{=}NH_2^+$ in HF solvent at −20 °C (top traces) and simulated spectrum (bottom traces). The daggers (†) in the experimental spectrum denote the $^1\Delta^{19}F(^{34/32}S)$ secondary isotope shifts.

Table 2. Summary of Crystal Data and Refinement Results for $[F_4S{=}NXe][AsF_6]$ and $[F_4S{=}NH_2][AsF_6]$

	$[F_4S{=}NXe][AsF_6]$	$[F_4S{=}NH_2][AsF_6]$
empirical formula	$F_{10}NSXeAs$	$F_{10}NSH_2As$
space group	$C2/c$ (No. 15)	$P\bar{1}$ (No. 2)
a (Å)	25.930(1)	5.4447(6)
b (Å)	5.0875(3)	6.6457(7)
c (Å)	14.8171(8)	10.306(1)
α (deg)	90	89.484(9)
β (deg)	119.549(1)	87.479(7)
γ (deg)	90	74.955(7)
V (Å^3)	1700.4(4)	359.79(9)
molecules/unit cell	8	2
mol wt (g mol^{-1})	442.29	313.00
calcd density (g cm^{-3})	3.455	2.889
T (°C)	−173	−173
μ (mm^{-1})	8.29	5.16
$R_1{}^a$	0.0224	0.0855
$wR_2{}^b$	0.0524	0.1725

^{a} R_1 is defined as $\sum||F_o| - |F_c||/\sum|F_o|$ for $I > 2\sigma(I)$. ^{b} wR_2 is defined as $[\sum[w(F_o^2 - F_c^2)^2]/\sum w(F_o^2)^2]^{1/2}$ for $I > 2\sigma(I)$.

are resolved, whereas its lower frequency counterpart has only six transitions resolved due to overlap of the inner transitions.

X-ray Crystal Structures of $[F_4S{=}NXe][AsF_6]$ and $[F_4S{=}NH_2][AsF_6]$. Summaries of the refinement results and other crystallographic information are provided in Table 2. Important bond lengths and angles for $[F_4S{=}NXe][AsF_6]$ and $[F_4S{=}NH_2][AsF_6]$ are listed in Table 3 along with the calculated gas-phase geometries of the $F_4S{=}NXe^+$ and $F_4S{=}NH_2^+$ cations. Experimental and calculated geometric parameters for the $[F_4S{=}NXe][AsF_6]$ ion pair are compared in Table S1, and the experimental geometric parameters for the AsF_6^- anions in $[F_4S{=}NH_2][AsF_6]$ are provided in Table S2. Both cation geometries are derived from trigonal bipyramidal VSEPR arrangements of bonding electron pairs about sulfur, with the nitrogen and two fluorine atoms in the equatorial plane and two fluorine atoms in axial positions.

(a) $[F_4S{=}NXe][AsF_6]$. In the crystal packing diagram of $[F_4S{=}NXe][AsF_6]$ (Figure 5), the structural units are stacked, without alternation of the cation and anion positions, along the *b*-axis, but the cation and anion positions alternate along the *a*- and *c*-axes so that the ion pairs align in a head-to-tail fashion in the *ac*-plane. The $F_4S{=}NXe^+$ cation and the AsF_6^- anion form an ion pair by interaction through a Xe---F—As fluorine bridge (Figure 6). The symmetry lowering experienced by the anion is shown in the crystal structure to be essentially an axial distortion of its O_h symmetry in which the four equatorial As−F bonds and the As−F bond trans to the elongated bridging As−F bond are equal to within $\pm 3\sigma$, giving approximate local C_{4v} symmetry.

The Xe−N bond length (2.084(3) Å) is similar to that of $[F_5SN(H)Xe][AsF_6]$ (2.069(4) Å)[6] and is only slightly longer than the Xe−N bond in $[F_5TeN(H)Xe][AsF_6]$ (2.044(4) Å).[7] The xenon atom lies in the N(1), S(1), F(1), F(4)-plane, and the bent S−N−Xe angle (118.0(2)°) is attributed to the stereochemically active valence electron lone pair on nitrogen. The S=N bond length (1.556(3) Å) is significantly longer than those of $F_4S{=}NF$ (1.520(9) Å)[14] and $F_4S{=}NCH_3$ (1.480(6) Å).[19] The axial S−F(1) bond (1.576(2) Å) anti to xenon is longer than those in $F_4S{=}NCH_3$ (1.546(7) Å)[19] and $F_4S{=}NF$ (1.535(12) Å),[14] while the *syn*-axial S−F(4) bond (1.588(2) Å) is shorter than the corresponding bonds in $F_4S{=}NCH_3$ (1.643(4) Å)[19] and $F_4S{=}NF$ (1.615(7) Å).[14] The equatorial S−F(2) and S−F(3) bond lengths (1.518(2) and 1.529(2) Å) are also significantly shorter than those of $F_4S{=}NCH_3$ (1.567(4) Å)[19] and $F_4S{=}NF$ (1.564(5) Å).[14]

The long contacts to xenon in the crystal structure may be grouped into three categories that are significantly less than the sum of the Xe and F van der Waals radii (3.63 Å):[34] (1) the short ion-pair contact, Xe---F (2.618(2) Å), which is trans to the Xe−N bond and very similar to the corresponding contacts in $[F_5SN(H)Xe][AsF_6]$ (2.634(3) Å)[6] and $[F_5TeN(H)Xe][AsF_6]$ (2.580(3) Å);[7] (2) three very similar contacts between fluorine atoms of the anion and xenon (F7A, 3.226(3); F9A, 3.226(3); F8A, 3.232(3) Å); and (3) three longer interionic contacts between xenon and fluorine atoms of the anion (F10A, 3.410(3); F7B, 3.452(3); F5A, 3.459(3) Å). The three contacts at 3.23 Å, when considered with the Xe−N bond and Xe---F ion pair

Table 3. Experimental Geometries for $[F_4S{=}NXe][AsF_6]$ and $[F_4S{=}NH_2][AsF_6]$ and Calculated Geometries for $F_4S{=}NXe^+$ and $F_4S{=}NH_2^+$ [a]

	$F_4S{=}NXe^+$				$F_4S{=}NH_2^+$			
		calcd (C_1)[b]				calcd (C_s)[c]		
	exptl	MP2	PBE1PBE	B3LYP	exptl	MP2	PBE1PBE	B3LYP
				Bond Lengths (Å)				
Xe(1)−N(1)	2.084(3)	2.063	2.120	2.183				
N(1)−S(1)	1.556(3)	1.583	1.582	1.595	1.511(6)	1.558	1.558	1.567
N(1)−H(1)					1.011[d]	1.013	1.013	1.014
N(1)−H(2)					1.012[d]	1.013	1.013	1.014
S(1)−F(1)	1.576(2)	1.573	1.576	1.594	1.564(5)	1.569	1.568	1.581
S(1)−F(2)	1.518(2)	1.536	1.534	1.547	1.511(5)	1.521	1.523	1.536
S(1)−F(3)	1.529(2)	1.536	1.534	1.547	1.526(5)	1.521	1.523	1.536
S(1)−F(4)	1.588(2)	1.604	1.592	1.605	1.558(5)	1.569	1.568	1.581
Xe(1)---F(5)	2.618(2)							
As(1)−F(5)	1.758(2)							
				Bond Angles (°)				
Xe(1)−N(1)−S(1)	118.0(2)	118.6	117.9	119.1				
S(1)−N(1)−H(1)					105.8[d]	119.0	119.1	119.1
S(1)−N(1)−H(2)					128.6[d]	119.0	119.1	119.1
H(1)−N(1)−H(2)					122.3[d]	122.0	121.7	121.8
N(1)−S(1)−F(1)	86.4(2)	85.7	84.4	83.9	92.6(3)	90.7	90.8	90.9
N(1)−S(1)−F(2)	127.3(2)	126.7	126.5	126.8	125.2(3)	125.3	125.2	125.2
N(1)−S(1)−F(3)	127.8(2)	126.7	126.5	126.8	126.3(3)	125.3	125.2	125.2
N(1)−S(1)−F(4)	100.1(2)	98.6	99.1	99.0	91.9(3)	90.7	90.8	90.9
F(1)−S(1)−F(2)	88.6(1)	89.4	89.4	89.5	88.7(3)	89.6	89.6	89.5
F(1)−S(1)−F(3)	87.9(1)	89.4	89.4	89.5	88.3(3)	89.6	89.6	89.5
F(1)−S(1)−F(4)	173.5(1)	175.7	176.5	177.1	175.5(3)	178.6	178.5	178.2
F(2)−S(1)−F(3)	104.3(1)	106.2	106.4	105.7	108.5(3)	109.4	109.5	109.5
F(2)−S(1)−F(4)	88.1(1)	88.0	88.5	88.8	88.9(3)	89.6	89.6	89.5
F(3)−S(1)−F(4)	87.5(1)	88.0	88.5	88.8	88.8(3)	89.6	89.6	89.5
N(1)−Xe(1)---F(5)	172.2(1)							
Xe(1)---F(5)−As(1)	148.6(1)							

[a] The labels correspond to those used in Figures 6 and 7. Geometric parameters for the AsF_6^- anions of $[F_4S{=}NXe][AsF_6]$ and $[F_4S{=}NH_2][AsF_6]$ are found in Tables S1 and S2, respectively. [b] aug-cc-pVTZ(-PP) basis set. [c] aug-cc-pVTZ basis set. [d] The hydrogen atom positions were calculated using a riding model; therefore, no estimated standard deviations are provided.

contact, form a distorted trigonal bipyramidal arrangement about Xe. The three equatorial fluorine contacts are not coplanar with Xe, which is displaced 1.226(2) Å out of the F7A, F8A, F9A-plane toward the nitrogen atom (Figure S1). Thus, the three F-contacts avoid the torus of xenon valence electron density that results from its three valence electron lone pairs.[42]

(b) $[F_4S{=}NH_2][AsF_6]$. The structure of $[F_4S{=}NH_2][AsF_6]$ consists of well-separated $F_4S{=}NH_2^+$ cations and AsF_6^- anions (Figure 7). There are two crystallographically independent anions which show little distortion from octahedral geometry, with As−F bonds ranging from 1.704(4) to 1.728(4) Å, in good agreement with previously reported values.[1,7] In the asymmetric unit, two half-occupancy arsenic atoms lie on inversion centers, with three fluorines defined on general positions for each arsenic atom, and the remaining three fluorines of each anion generated by symmetry. All atoms of the cation are on general positions. A distorted square planar arrangement of four fluorines from four different anions has close cation-anion N---F contacts (F10A, 2.824(3); F6, 2.841(3); F8, 2.916(3); F5A, 2.925(3) Å), which are less than the sum of the nitrogen and fluorine van der Waals radii (3.02 Å)[34] and result in a distorted square pyramidal arrangement with nitrogen at the apex and at a distance of 1.770(5) Å for its normal to the F10A, F6, F8, F5A-plane.

Although the electron densities and the three equatorial bond lengths were similar, the S=N bond could be differentiated on the basis of the three equatorial bond angles; i.e., two F−S−N angles were equal within experimental error, with the third, smaller angle corresponding to the F−S−F angle. The crystallographic positions of the hydrogen atoms were calculated and therefore are not discussed.

The S=N bond length (1.511(6) Å) of $F_4S{=}NH_2^+$ is bracketed by those of $F_4S{=}NCH_3$ (1.480(6) Å)[19] and $F_4S{=}NF$ (1.520(9) Å)[14] and is significantly shorter than that of $F_4S{=}NXe^+$ (vide supra). The axial S−F(1) and S−F(4) bond lengths (1.564(5) and 1.558(5) Å) of $F_4S{=}NH_2^+$ are the same within experimental error and are significantly shorter than those in $F_4S{=}NXe^+$ (vide supra) and in isoelectronic $F_4S{=}CH_2$ (1.595(2) and 1.592(2) Å),[43] and $F_4S{=}O$ (1.596(4) Å).[44] Similarly, the equatorial S−F(2) and S−F(3) bond lengths (1.511(5) and 1.526(5) Å) are the same, within experimental error, and comparable to those in $F_4S{=}NXe^+$ (vide supra) and $F_4S{=}O$ (1.533(4) Å),[44] while they are significantly shorter than those of $F_4S{=}CH_2$ (1.560(2) and 1.561(2) Å).[43]

Raman Spectroscopy. The Raman spectrum of $[F_4S{=}NXe][AsF_6]$ (Figure 8) was assigned by comparison with those of $F_4S{=}NF$ (Table S3) and AsF_6^-,[6] and with those calculated for the gas-phase $F_4S{=}NXe^+$ cation (Table 4 and Computational Results) and the gas-phase $[F_4S{=}NXe][AsF_6]$ ion pair (Table S4) at several levels of theory. Calculated frequencies at the MP2/aug-cc-pVTZ(-PP) level provided the best overall agreement with the experimental values (see Computational Results) and are considered in the ensuing discussion (indicated in square brackets). The $[F_4S{=}NXe][AsF_6]$ ion pair geometry and vibrational frequencies were calculated at the MP2/(SDB-)cc-pVTZ level.

(42) Mercier, H. P. A.; Moran, M. D.; Sanders, J. C. P.; Schrobilgen, G. J.; Suontamo, R. J. *Inorg. Chem.* **2005**, *44*, 49–60.

(43) Simon, A.; Peters, E. M.; Lentz, D.; Seppelt, K. *Z. Anorg. Allg. Chem.* **1980**, *468*, 7–14.

(44) Gundersen, G.; Hedberg, K. *J. Chem. Phys.* **1969**, *51*, 2500–2507.

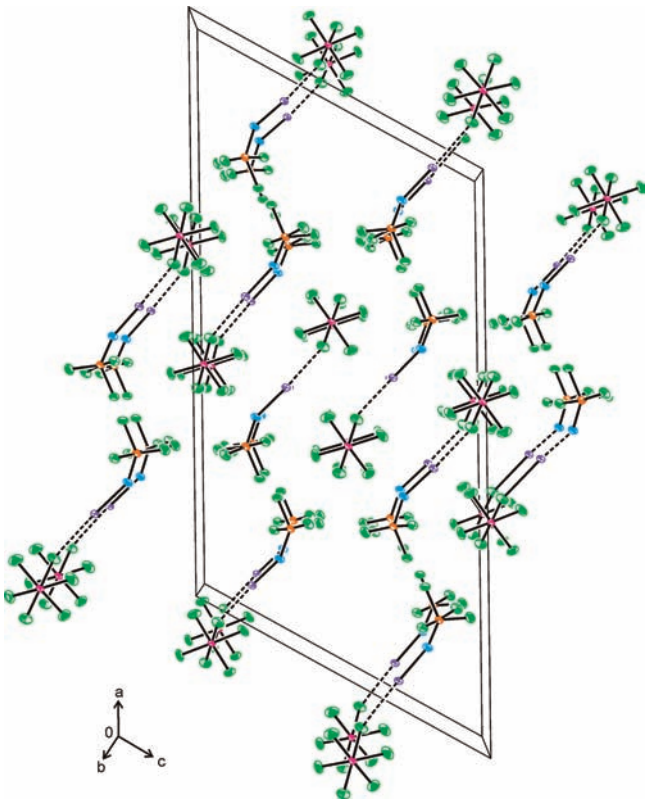

Figure 5. Packing diagram for the X-ray crystal structure of $[F_4S{=}NXe][AsF_6]$ viewed along the *b*-axis. Thermal ellipsoids are shown at the 50% probability level.

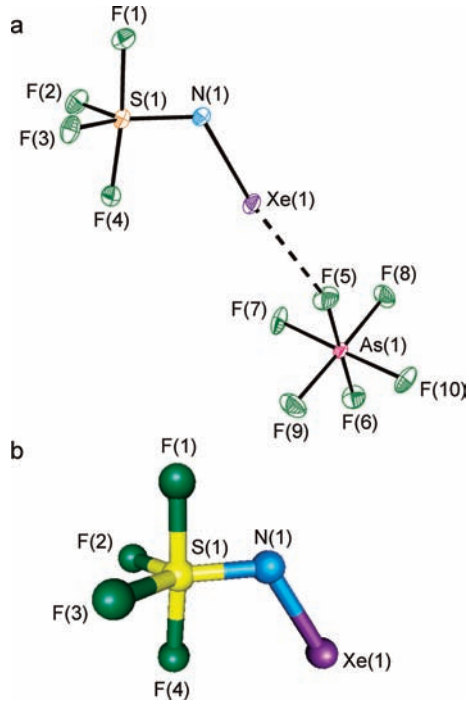

Figure 6. (a) Structural unit in the X-ray crystal structure of $[F_4S{=}NXe][AsF_6]$; thermal ellipsoids are shown at the 50% probability level. (b) Calculated geometry (MP2/aug-cc-pVTZ(-PP)) of the $F_4S{=}NXe^+$ cation.

The 15 vibrational modes of $F_4S{=}NXe^+$ have been assigned under C_1 symmetry, in accord with the energy-minimized

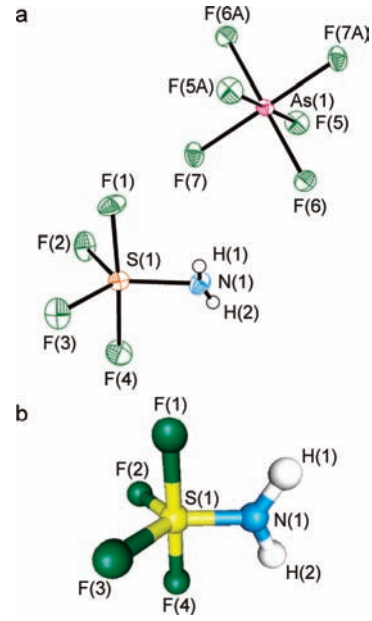

Figure 7. (a) Structural unit in the X-ray crystal structure of $[F_4S{=}NH_2][AsF_6]$; the hydrogen atom positions are calculated, and the thermal ellipsoids of the non-hydrogen atoms are shown at the 50% probability level. (b) Calculated geometry (MP2/aug-cc-pVTZ) of the $F_4S{=}NH_2^+$ cation.

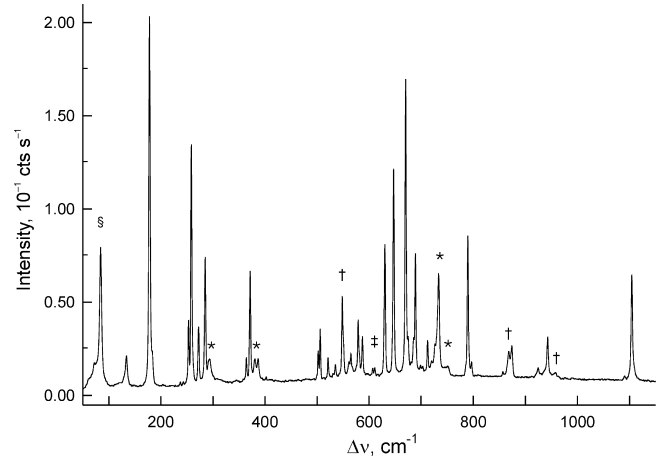

Figure 8. Raman spectrum of $[F_4S{=}NXe][AsF_6]$, formed by solid-state rearrangement of $[F_3S{\equiv}NXeF][AsF_6]$ for 70 min at 22 °C, recorded at −160 °C using 1064-nm excitation. Symbols denote peaks from unreacted $[F_3S{\equiv}NXeF][AsF_6]$ (†), ν(XeF) of unreacted $[XeF][AsF_6]$ (‡), an instrumental artifact (§), and FEP sample tube bands (*).

geometry, rather than the ideal C_s symmetry expected for the gas-phase cation (see Computational Results). Accordingly, all modes belong to A irreducible representations and are both Raman- and infrared-active. The fluorine bridge between the cation and anion (see X-ray Crystal Structure of $[F_4S{=}NXe][AsF_6]$) lowers the anion symmetry, giving rise to additional lines in the vibrational spectrum. Symmetry lowering of the anion can be approximated by local C_{4v} symmetry,[45] and the vibrational spectra can be assigned under this or a lower symmetry (C_{2v}, C_s, or C_1). In the present study, the anion modes have been assigned under local C_{4v} symmetry, which

(45) Lehmann, J. F.; Dixon, D. A.; Schrobilgen, G. J. *Inorg. Chem.* **2001**, *40*, 3002–3017.

Table 4. Raman Frequencies and Intensities for $[F_4S{=}NXe][AsF_6]$ and Calculated Vibrational Frequencies, Intensities, and Assignments for $F_4S{=}NXe^+$

freq, cm^{-1}					
	calcd[b]			assgnts[c]	
exptl[a]	MP2	PBE1PBE	B3LYP	$F_4S{=}NXe^+$ (C_1)	AsF_6^- (C_{4v})
1104 (29)	1102 (5) [322]	1077 (15) [297]	1020 (19) [283]	ν(S=N)	
1097 (1)					
943 (11)	958 (2) [173]	962 (3) [173]	919 (3) [169]	ν(SF2 – SF3)	
924 (2)					
874 (8)	903 (8) [286]	908 (11) [285]	863 (13) [279]	ν(SF1 – SF4)	
857 (1)					
796 (4)	806 (12) [82]	789 (12) [52]	744 (13) [47]	ν(SF2 + SF3 + SF4) + ν(S=N)	
789 (38)					
726 sh					ν_8 (E)
712 (9)					
689 (32)					ν_1 (A_1)
675 sh	664 (17) [23]	614 (16) [36]	588 (16) [30]	δ(NSF2F3) o.o.p.	
670 (79)					
647 (55)	645 (8) [7]	658 (5) [2]	632 (5) [3]	ν(SF1 + SF4)	
630 (35)					
587 (11)					ν_2 (A_1)
579 (15)					ν_5 (B_1)
565 (6)	578 (1) [30]	565 (3) [33]	545 (3) [26]	δ(NSF1) – δ(NSF4) + ρ_w(F2SF3)[d]	
561 (3)					
535 (3)	554 (1) [65]	546 (3) [11]	525 (4) [124]	δ(F1SF4) + δ(F2SF3)	
530 sh					
521 (5)	508 (1) [<1]	502 (1) [1]	483 (1) [1]	δ(F1SF2) + δ(F3SF4)	
506 (13)	497 (2) [17]	494 (2) [17]	474 (2) [15]	δ(NSF1F4) o.o.p. + ρ_r(F2SF3)	
502 (7)					
402 (1)					ν_4 (A_1)
387 (6)					ν_3 (A_1)
371 (30)					ν_7 (B_2)
364 (7)					ν_9 (E)
346 (1) br	450 (4) [20][e,f]	424 (2) [82][e]	400 (3) [46][e]	ν(As–F5)[e]	
	441 (1) [129][e,f]	416 (4) [76][e]	411 (6) [104][e]	ν(Xe--F5)[e]	
285 (35)	256 (2) [1]	272 (2) [1]	263 (1) [<1]	δ(F1SF4) + δ(F2SF3)[d]	
273 (16)	255 (1) [1]	259 (1) [1]	251 (1) [1]	δ(XeNS) o.o.p. + δ(NSF2) – δ(NSF3)	
259 (65)	288 (3) [<1]	245 (4) [5]	226 (4) [6]	ν(XeN)	
253 (18)					
184 sh	166 (5) [<1]	149 (7) [1]	135 (9) [2]	δ(XeNS) i.p.	
178 (100)					
134 (8)	97 (1) [<1]	94 (1) [<1]	90 (1) [<1]	torsion about Xe–N bond	

[a] Values in parentheses denote experimental Raman intensities, and abbreviations denote shoulder (sh) and broad (br). [b] aug-cc-pVTZ(-PP) basis set. Calculated Raman intensities ($Å^4$ amu^{-1}) are given in parentheses, and calculated infrared intensities (km mol^{-1}) are given in square brackets. [c] Abbreviations denote out of plane (o.o.p.), in plane (i.p.) (planes are defined by the atoms they contain), wag (ρ_w), and rock (ρ_r). The anion symmetry, C_{4v}, is an approximate local symmetry resulting from a short anion-cation fluorine bridge contact. [d] The coupled δ(NSF4) bend calculated at the MP2 level does not contribute to the split band at 561, 565 cm^{-1}, but it does contribute to the band at 285 cm^{-1}. [e] Values and mode descriptions are for the calculated ion pair; see Table S4 for a full frequency listing and assignments. [f] (SDB-)cc-pVTZ basis set.

is expected to result in 15 fundamental vibrational modes belonging to the irreducible representations $4A_1 + 2B_1 + B_2 + 4E$, all of which are Raman-active, with the A_1 and E modes also infrared-active. In practice, 8 of the 11 predicted vibrational bands were observed in the Raman spectrum (correlations with O_h symmetry are given in square brackets): 689 (A_1) and 712, 726 (E) [T_{1u}], 579 (B_1) and 587 (A_1) [E_g], 387 (A_1) and 402 (A_1) [T_{1u}], and 364 (E) and 371 (B_2) [T_{2g}] cm^{-1}. Factor-group analyses correlating the free cation (C_s) and distorted local anion (C_{4v}) symmetries to their crystal site symmetries (C_1) and to the unit cell symmetry (C_{2h}) are provided in Table S5. The A′ and A″ irreducible representations of the C_s gas-phase cation correlate to A irreducible representations under C_1 site symmetry, while the doubly degenerate E-modes of the anion are split due to site symmetry lowering. Both the cation and anion bands are split into Raman-active A_g and B_g components and infrared-active A_u and B_u components under C_{2h} crystal symmetry, giving the potential to observe a total of 30 bands for the cation and 30 bands for the anion. It proved possible to resolve this splitting in the Raman spectrum for 11 of the 15 observed cation bands and for one anion band.

The ν(XeN) stretching frequency at 253, 259 [288] cm^{-1} is similar to that observed in $F_5SN(H)Xe^+$ (224 cm^{-1}).[6] The most intense band in the Raman spectrum of $[F_4S{=}NXe][AsF_6]$ occurs at 178, 184 [166] cm^{-1} and is assigned to the in-plane Xe−N−S bend, which compares well with the strong band observed at 150 cm^{-1} for $F_5SN(H)Xe^+$.[6] The out-of-plane Xe−N−S bend at 273 [255] cm^{-1} and the in-plane Xe−N−S bend bracket the Xe−N−S bends reported for $XeN(SO_2F)_2^+$ (226, 241, 251, 259, 267 cm^{-1})[12] and $F[XeN(SO_2F)_2]_2^+$ (208, 224, 231, 240, 247, 260, 264 cm^{-1})[12] which are all higher in frequency than those of $FXeN(SO_2F)_2$ (96, 111, 116, 119 cm^{-1}).[10] Although no ν(XeN) stretch was reported for $XeN(SO_2F)_2^+$,[12] it now appears likely, based on the assigned frequencies of $F_4S{=}NXe^+$ and $F_5SN(H)Xe^+$,[6] that at least one of the bands previously assigned to δ(XeNS) in $XeN(SO_2F)_2^+$ is, in fact, the ν(XeN) stretch, namely, the band at 251 cm^{-1}. The S=N stretch at 1097, 1104 [1102] cm^{-1} is in good agreement with that of $F_4S{=}NF$ (1125 cm^{-1})[14] and is lower in frequency than those of $F_4S{=}NSF_5$ (1299 cm^{-1})[26] and $F_4S{=}NCF_3$ (1343 cm^{-1}).[22] The broad, low-intensity band at 346 cm^{-1} could not be assigned by comparison with the modes calculated for the $F_4S{=}NXe^+$ cation, and was assigned to ν(Xe---F) by comparison with its counterparts in $[XeN(SO_2F)_2][AsF_6]$ (317 cm^{-1}),[12] $[XeOTeF_5][AsF_6]$ (365 cm^{-1}),[42,46] and $[XeF][AsF_6]$ (417 cm^{-1}).[47] The ν(Xe---F) stretching frequency calculated for the $[F_4S{=}NXe][AsF_6]$ ion pair [441 cm^{-1}] was significantly higher, which is in accordance with the underestimated Xe---F distance obtained for the calculated ion-pair geometry (vide supra; also see Table S1). The experimental SF_4 stretches (670−958 cm^{-1}) and bends (285−647 cm^{-1}) fall into ranges that are similar to those of the benchmark, $F_4S{=}NF$.[14] The low-intensity band at 134 [97] cm^{-1} is assigned to the torsional motion of the $F_4S{=}N$-group about the Xe−N bond. No other calculated low-frequency anion bands or coupled deformation bands of the cation could be observed in the experimental spectrum.

Computational Results. Quantum-chemical calculations were carried out for $F_4S{=}NH_2^+$, $F_4S{=}NXe^+$, and the $[F_4S{=}NXe][AsF_6]$ ion pair, using B3LYP, PBE1PBE, and MP2 methods to support the vibrational assignments (see Raman Spectroscopy) and to gain insight into their structures and bonding (Tables 3 and S1). Comparison of the calculated and experimental frequencies for the benchmark, $F_4S{=}NF$, showed that the B3LYP calculations provided vibrational frequencies that were in better agreement for the S−N stretches, while the MP2 frequencies were in better agreement for the S−F stretching and F−S−F bending frequencies (Table S3). Assignments of the $F_4S{=}N$-group modes in $F_4S{=}NXe^+$ were made taking these trends into account (see Raman Spectroscopy). The best overall agreement (geometric parameters and vibrational frequencies) for the species discussed in this work was obtained for the MP2 calculations, using the aug-cc-pVTZ-(-PP) basis set for the cations, and (SDB-)cc-pVTZ for the ion pair. These values are referred to in the subsequent discussion and appear in square brackets.

(a) Calculated Geometries. Although very close to C_s symmetry, the MP2, PBE1PBE, and B3LYP energy-minimized geometries of the $F_4S{=}NH_2^+$ and $F_4S{=}NXe^+$ cations and the $[F_4S{=}NXe][AsF_6]$ ion pair optimized to C_1 symmetry. For $[F_4S{=}NXe][AsF_6]$, the largest discrepancies occurred for the fluorine bridge, Xe---F−As. The calculated Xe---F and As−F fluorine-bridge bond lengths [2.309 and 1.867 Å] are under- and overestimated when compared with their respective experimental values, 2.618(2) and 1.758(2) Å. The calculated Xe---F bond order [0.11] is consistent with weak covalent bonding when compared with the bond order [0.53] of the Xe−N bond. The Xe---F−As angle, found to be bent in the low-temperature X-ray crystal structure (148.5(1)°), differs significantly from that of the calculated geometry [116.2°]. This is expected because this angle is very deformable and easily influenced by crystal packing. The deformability of this angle is supported by the calculated δ(Xe---F−As) frequencies, which occur at very low values [62, 85 cm^{-1}]. Similar discrepancies have been found between the Xe---F−As angles for the calculated ion pairs, $[F_5SN(H)Xe][AsF_6]$[6] and $[F_5TeN(H)Xe][AsF_6]$,[7] and those in their crystal structures. It is noteworthy that the calculated local symmetry of AsF_6^- in $[F_4S{=}NXe][AsF_6]$ is better approximated by C_{2v} symmetry than by the local C_{4v} symmetry used to assign the vibrational frequencies of AsF_6^- in the ion pair. Local C_{4v} symmetry was employed for vibrational assignments because the AsF_6^- anion closely approximates this symmetry in the X-ray crystal structure (see section on the X-ray crystal structure of $[F_4S{=}NXe][AsF_6]$ and Raman Spectroscopy). In general, calculated S=N bond lengths were longer, and calculated S−F bond lengths were longer or the same within the error limits of the experimental bond lengths for the $F_4S{=}NF$, $F_4S{=}NXe^+$, and $F_4S{=}NH_2^+$ cations (see Calculated Geometries). In the calculated $F_4S{=}NH_2^+$ geometry, the hydrogen atoms are in the plane of the N, S, and axial F atoms, in agreement with the ^{19}F NMR spectrum (see NMR Spectroscopy), establishing that the $F_4S{=}NH_2^+$ cation is isostructural with the isoelectronic $F_4S{=}CH_2$ molecule. The hydrogen positions of $F_4S{=}NH_2^+$ could not, however, be determined by single-crystal X-ray diffraction where a riding model was used to calculate their crystallographic positions.

The S=N bond length in $F_4S{=}NXe^+$ is predicted to be 0.025 Å longer than that of $F_4S{=}NH_2^+$, and the S−F bond lengths are also predicted to be longer, i.e., S−F(1) 0.004, S−F(2) 0.015, S−F(3) 0.015, and S−F(4) 0.035 Å. This trend is in agreement with the experimental S=N bond length of $F_4S{=}NXe^+$, which is 0.045(9) Å longer than that of $F_4S{=}NH_2^+$, and with the experimental S−F(4) bond length, which is longer by 0.030(7) Å. These longer bond lengths are attributed to the steric effect of the xenon atom (see Comparison of $F_4S{=}NXe^+$ and $F_4S{=}NH_2^+$ with Related $F_4S{=}ERR'$ Derivatives and SF_4). The experimental trends for $F_4S{=}NXe^+$ and $F_4S{=}NH_2^+$ cannot be commented upon for the S−F(1), S−F(2), and S−F(3) bond lengths because they are the same within $\pm 3\sigma$.

(b) Calculated Frequencies. The calculated vibrational frequencies and intensities of $F_4S{=}NXe^+$ were used to assist in the assignment of the experimental Raman frequencies (see Table 4 and Raman Spectroscopy), and although the Raman spectrum of $[F_4S{=}NH_2][AsF_6]$ could not be recorded (see Syntheses of $[F_4S{=}NXe][AsF_6]$ and $[F_4S{=}NH_2][AsF_6]$), the vibrational frequencies were calculated (Table S6) and compared with the calculated frequencies of $F_4S{=}NXe^+$. All calculated stretching frequencies of the $F_4S{=}NH_2^+$ cation are shifted to significantly higher frequencies than the corresponding frequencies of $F_4S{=}NXe^+$: ν(S=N), [+69 cm^{-1}]; ν(SF2 − SF3), [+53 cm^{-1}]; ν(SF1 − SF4), [+29 cm^{-1}]; ν(SF2 + SF3 + SF4) + ν(S=N), [+31 cm^{-1}]; and ν(SF1 + SF4), [+40 cm^{-1}]. In contrast, there is no single trend for the calculated bending modes; i.e., the in-phase F−S−F bends are shifted to higher

(46) Keller, N.; Schrobilgen, G. J. *Inorg. Chem.* **1981**, *20*, 2118–2129.
(47) Gillespie, R. J.; Landa, B. *Inorg. Chem.* **1973**, *12*, 1383–1388.

Table 5. Geometrical Parameters and Natural Bond Orbital Charge, Valencies, and Bond Orders for the $F_4S{=}E-$ Moieties of $F_4S{=}CH_2$, $F_4S{=}NH_2^+$, $F_4S{=}NXe^+$, $F_4S{=}NCH_3$, $F_4S{=}NF$, and $F_4S{=}O$ and for SF_4[a]

Geometrical Parameters

	$F_4S{=}CH_2$		$F_4S{=}NH_2^+$		$F_4S{=}NXe^+$		$F_4S{=}NCH_3$		$F_4S{=}NF$		$F_4S{=}O$		SF_4	
param	exptl[43]	calcd	exptl[b]	calcd	exptl[b]	calcd	exptl[19]	calcd	exptl[14]	calcd	exptl[44]	calcd	exptl[48]	calcd
$S-F_B$ (Å)	1.595(2)	1.617	1.564(5)	1.569	1.576(2)	1.573	1.546(7)	1.599	1.535(12)	1.591	1.596(4)	1.614	1.646(3)	1.664
$S-F_X$ (Å)	1.592(2)		1.558(5)		1.588(2)	1.604	1.643(4)	1.648	1.615(7)	1.598				
$S-F_A$ (Å)	1.561(2)	1.582	1.511(5)	1.521	1.518(2)	1.536	1.567(4)	1.578	1.564(5)	1.568	1.533(4)	1.558	1.545(3)	1.561
	1.560(2)		1.526(5)		1.529(2)									
S=E (Å)	1.554(4)	1.586	1.511(6)	1.558	1.556(3)	1.583	1.480(6)	1.505	1.520(9)	1.570	1.405(4)	1.425		
F_A-S-F_A (°)	96.8(1)	97.2	108.5(3)	109.4	104.3(1)	106.2	102.6(2)	102.6	99.8(3)	100.3	114.9(34)	111.9	101.5(5)	101.5
F_B-S-F_X (°)	170.5(1)	171.7	175.5(3)	178.6	173.5(1)	175.7	167.0(6)	167.0	172.5(7)	173.7	164.4(6)	164.5	173.1(5)	172.2
$E{=}S-F_A$ (°)	131.4(2)	131.4	125.2(3)	125.3	127.3(2)	126.7	128.7(4)	128.7	130.1(6)	129.7	122.5(17)	124.1	129.3(5)	129.3
	131.7(2)		126.3(3)		127.8(2)									
$E{=}S-F_X$ (°)	94.7(2)	94.1	91.9(3)	90.7	100.1(2)	98.6	98.4(4)	99.3	96.9(4)	98.6	97.8(3)	97.7	93.4(5)	93.9
$E{=}S-F_B$ (°)	94.9(2)	94.1	92.6(3)	90.7	86.4(2)	85.7	94.6(4)	93.8	90.6(5)	87.7	97.8(3)	97.7	93.4(5)	93.9
$E{=}S-F_X - E{=}S-F_B$ (°)	−0.2(4)	0	−0.7(6)	0	13.7(4)	12.9	3.8(8)	5.5	6.3(9)	10.9	0	0	0	0
$QA_{\angle E=S-F}$ (°)	113.2(4)	112.8	109.0(6)	108.0	110.4(4)	109.4	112.6(7)	112.6	111.9(9)	111.4	110.2(18)	110.9	111.4(9)	111.6

NBO Analysis

	$F_4S{=}CH_2$		$F_4S{=}NH_2^+$		$F_4S{=}NXe^+$		$F_4S{=}NCH_3$		$F_4S{=}NF$		$F_4S{=}O$		SF_4	
atom	charge	val	charge	val	charge	val	charge	val	charge	val	charge	val	charge	val
F_B	−0.49	0.52	−0.43	0.51	−0.40	0.62	−0.47	0.55	−0.45	0.59	−0.48	0.43	−0.55	0.41
F_A	−0.45	0.53	−0.36	0.55	−0.38	0.65	−0.44	0.56	−0.43	0.59	−0.42	0.50	−0.45	0.54
F_X	−0.49	0.52	−0.43	0.51	−0.47	0.56	−0.51	0.49	−0.47	0.56	−0.48	0.43	−0.55	0.41
S	2.27	3.81	2.61	3.52	2.50	4.07	2.47	3.92	2.38	3.90	2.62	3.47	2.00	2.16
E	−0.86	2.73	−0.96	2.23	−0.87	1.67	−0.83	1.90	−0.37	1.70	−0.81	1.00		

Bond Order

bond	$F_4S{=}CH_2$	$F_4S{=}NH_2^+$	$F_4S{=}NXe^+$	$F_4S{=}NCH_3$	$F_4S{=}NF$	$F_4S{=}O$	SF_4
S=E	1.28	0.99	1.18	1.15	1.31	1.20	
$S-F_B$	0.61	0.61	0.69	0.55	0.65	0.66	0.46
$S-F_A$	0.65	0.67	0.76	0.61	0.68	0.70	0.62
$S-F_X$	0.61	0.61	0.66	0.55	0.60	0.66	0.46

[a] Where E = C, N, O. All calculations at the MP2/aug-cc-pVTZ(-PP) level of theory. The fluorine atom labeling schemes are given by structures I and II. $QA_{\angle E=S-F}$ is the quadruple average angle,[49] defined as the average of the four possible E=S−F (:−S−F, in the case of the SF_4) angles. [b] This work.

frequency (δ(F1SF4) + δ(F2SF3), [+26 cm^{-1}]; δ(F1SF2) + δ(F3SF4), [+6 cm^{-1}]) and the out-of-phase bend is effectively unshifted (δ(F1SF4) − δ(F2SF3), [+1 cm^{-1}]). In addition, modes involving N are shifted to lower frequency (δ(NSF2F3) o.o.p., [−82 cm^{-1}]; δ(F1SN) − δ(F4SN), [−43 cm^{-1}]) except for δ(NSF1F4) o.o.p., [−1 cm^{-1}], which is essentially unshifted.

(c) Comparison of Charges, Valencies, and Bond Orders among the $F_4S{=}NXe^+$, $F_4S{=}NH_2^+$, $F_5SN(H)Xe^+$, and $F_5TeN(H)Xe^+$ Cations. The natural bond orbital (NBO) charges, valencies, and bond orders calculated by the MP2, PBE1PBE, and B3LYP methods (MP2 values are reported in square brackets) for $F_4S{=}NXe^+$ and $F_4S{=}NH_2^+$ are listed in Table S7, and those for $F_5SN(H)Xe^+$ and $F_5TeN(H)Xe^+$ are listed in Table S8. Positive charges in both $F_4S{=}NXe^+$ and $F_4S{=}NH_2^+$ reside on S, H, and Xe, with the positive charge on S [2.50] in $F_4S{=}NXe^+$ being slightly less than that in $F_4S{=}NH_2^+$ [2.61]. The Xe−N bond order of the $F_4S{=}NXe^+$ cation [0.59] is significantly greater than that of $F_3S{\equiv}NXeF^+$ [0.29] and essentially the same as those calculated for $F_5SN(H)Xe^+$ [0.60] and $F_5TeN(H)Xe^+$ [0.62], indicating considerable and comparable covalent bonding between xenon and nitrogen, which is in agreement with the Xe−N bond covalency trend inferred from the ^{129}Xe NMR chemical shifts for these species (see NMR Spectroscopy). Although not reflected in the calculated or experimental bond lengths, a decrease in the charge difference for sulfur and nitrogen in $F_4S{=}NXe^+$ is consistent with the greater S−N bond covalency and higher bond order of this bond [1.18] compared to that of $F_4S{=}NH_2^+$ [0.99].

Higher negative charges and lower valencies for the fluorine ligands of $F_4S{=}NXe^+$ are consistent with the lower S−F bond orders when compared with those of $F_4S{=}NH_2^+$. The charges, valencies, and bond orders for the benchmark, $F_4S{=}NF$, are in better agreement with those of $F_4S{=}NXe^+$ than with those of $F_4S{=}NH_2^+$, which is consistent with the presence of strongly electron-withdrawing substituents at N in the former cases.

(d) Comparison of $F_4S{=}NXe^+$ and $F_4S{=}NH_2^+$ with Related $F_4S{=}ERR'$ Derivatives and SF_4. The experimental and calculated geometries of $F_4S{=}NXe^+$, $F_4S{=}NH_2^+$, $F_4S{=}CH_2$, $F_4S{=}NCH_3$, $F_4S{=}NF$, $F_4S{=}O$, and SF_4 are compared in Table 5 along with their NBO charges, valencies, and bond orders. There is overall very good agreement between the calculated geometrical parameters, with all trends within the series being reproduced. The natural population analyses (NPA) reveal that the sulfur d orbital population ranges from 0.22 to 0.24 e for the $F_4S{=}ERR'$ species and is 0.17 for SF_4, so that the S−E bonds may be regarded as essentially pπ-pπ bonds.

(48) Tolles, W. M.; Gwinn, W. D. *J. Chem. Phys.* **1962**, *36*, 1119–1121.
(49) Hargittai, I. *J. Mol. Struct.* **1979**, *56*, 301–303.

Although the $F_4S{=}NXe^+$ cation may be expected to exhibit shorter, more covalent bonds than its neutral homologues, this is only apparent within the margins of experimental error for axial S—F_X and equatorial S—F_A bond length comparisons. Moreover, the S=N bond is longer and more polar than in $F_4S{=}NF$, which is in accordance with the smaller negative charge on nitrogen in $F_4S{=}NF$ than in $F_4S{=}NXe^+$ and correspondingly greater difference in sulfur and nitrogen charges for $F_4S{=}NXe^+$. The $F_4S{=}NXe^+$ cation follows the axial bond length trend of $F_4S{=}NF$ and $F_4S{=}NCH_3$, i.e., S—F_B < S—F_X. The S—F_B and S—F_X bond lengths are nearly equal, within experimental error for $F_4S{=}NXe^+$, but the S—F_X bond is significantly longer and the S—F_B bond is significantly shorter in $F_4S{=}NCH_3$ and $F_4S{=}NF$ (vide infra).

Comparison of $F_4S{=}NXe^+$ and $F_4S{=}NH_2^+$ reveals that the F_A—S—F_A and F_B—S—F_X angles are more compressed in $F_4S{=}NXe^+$ than in their $F_4S{=}NH_2^+$ counterparts. More insight is gained when the component angles N=S—F_X (100.1(2)°) and N=S—F_B (86.4(2)°) are considered for $F_4S{=}NXe^+$ and their difference, $\Delta(N{=}S{-}F_{axial}) = \angle N{=}S{-}F_X - \angle N{=}S{-}F_B$ (13.7(4)°), is considered. There is a significant interaction between the Xe and F_X atoms, with a Xe---F_X contact (2.824(8) Å) that is significantly less than the sum of the Xe and F van der Waals radii (3.63 Å), causing $\angle N{=}S{-}F_X$ to be more open and $\angle N{=}S{-}F_B$ to be more closed. Interestingly, the NBO analysis provides a negligible bond order (0.01) in this case; thus, the interaction is essentially Coulombic in nature, and the short contact is presumably a partial consequence of the nonspherical (toroidal) distribution of the valence electron density arising from the three valence electron lone pairs of xenon.[42] The slight lengthening of the S—F_X bond with respect to the S—F_B bond, which is also observed for the calculated geometry, is also consistent with a weak Coulombic interaction between F_X and the positive xenon center.

A steric interaction also occurs between F_X and the fluorine bonded to nitrogen in $F_4S{=}NF$ (F_N---F_X, 2.377(9) Å; sum of the fluorine van der Waals radii, 2.94 Å), with $\Delta(N{=}S{-}F_{axial}) = 6.3(9)°$ and $\angle N{=}S{-}F_X$ (96.9(4)°) again being more open than $\angle N{=}S{-}F_B$ (90.6(5)°). The F_A—S—F_A and F_B—S—F_X angles of $F_4S{=}NF$ are more compressed than those of either $F_4S{=}NXe^+$ or $F_4S{=}NH_2^+$, with the F_A—S—F_A angle showing the greater compression. This is consistent with a higher π electron density in the equatorial $F_2S{=}N$-plane of $F_4S{=}NF$ and a higher S—N bond covalency that is corroborated by the S—N bond order (1.31) and a correspondingly lower charge difference between sulfur and nitrogen (2.75 e) when compared with those of $F_4S{=}NXe^+$ (S—N b.o., 1.18; c.d., 3.37 e) and $F_4S{=}NH_2^+$ (S—N b.o., 0.99; c.d., 3.57 e). Comparisons with $F_4S{=}NF$ and $F_4S{=}CH_2$ show that the latter molecules exhibit the greatest F_A—S—F_A angle compressions within the series considered. The angle compressions and high S=N and S=C bond orders are again consistent with their charge differences and bond orders, S—C (b.o., 1.28; c.d., 3.13 e) and S—N (b.o., 1.31; c.d., 2.75 e), and with greater π S—E density in the equatorial $F_2S{=}E$-plane.

Although $\Delta(N{=}S{-}F_{axial})$ for $F_4S{=}NCH_3$ is considerably less than those for $F_4S{=}NXe^+$ and $F_4S{=}NF$, the difference is significant and is likely a consequence of the F_X---CH_3 steric interaction. The axial bond length differences for $F_4S{=}NF$ and $F_4S{=}NCH_3$ are significantly greater than that of $F_4S{=}NXe^+$, which is consistent with the strongly repulsive natures of the former steric interactions.

The $F_4S{=}CH_2$ molecule exhibits one of the most open F_B—S—F_B angles and, at the same time, one of the most compressed F_A—S—F_A angles among the $F_4S{=}ERR'$ (where R = R′) species considered in Table 5. The asymmetries of the S=C[43] and S=N bonds place most of the π bond electron density in the equatorial plane, which results in greater compression of the F_A—S—F_A angle than of the axial F_B—S—F_B angle. The greater degree of bond angle compression for both F—S—F angles in $F_4S{=}CH_2$ is presumably a consequence of the greater covalent character of the S=C bond (b.o. 1.28, compared to 0.99 for isoelectronic $F_4S{=}NH_2^+$), which results in greater double bond domain-single bond domain repulsions.

Following Hargittai,[49] the quadruple averages of angles E=S—F_A (2×), E=S—F_B, and E=S—F_X (where $\angle E{=}S{-}F_B = \angle E{=}S{-}F_X$ for $F_4S{=}CH_2$, $F_4S{=}NH_2^+$, $F_4S{=}O$, and SF_4) were evaluated and are compared in Table 5. The parameter, $QA_{\angle E=S-F}$, serves as a relative measure of the average spatial requirements of the double bond domains among the $F_4S{=}ERR'$ series and the lone pair domain of SF_4. The VSEPR rule-of-thumb, which states that a double bond domain and a lone pair domain have very similar spatial requirements,[50] is supported by the series under consideration, with the SF_4 value occurring approximately midway in the range and with a quadruple average E=S—F angle that is very similar to that of $F_4S{=}NF$. As expected for cations in this series, the $QA_{\angle E=S-F}$ values and spatial requirements of the S—N double bond domains of $F_4S{=}NXe^+$ and $F_4S{=}NH_2^+$, which are most similar to those of $F_4S{=}O$, are significantly less than those of the neutral molecules $F_4S{=}CH_2$, $F_4S{=}NCH_3$, and $F_4S{=}NF$.

Conclusions

The $F_4S{=}NXe^+$ cation has been synthesized by both solid-state rearrangement and HF solvolysis of the $F_3S{\equiv}NXeF^+$ cation. The discovery of the $F_4S{=}NXe^+$ cation as an intermediate in the HF solvolysis of the $F_3S{\equiv}NXeF^+$ cation en route to $F_5SN(H)Xe^+$ has served to significantly enhance our understanding of the reaction pathways that lead to $F_4S{=}NXe^+$ and $F_5SN(H)Xe^+$. Two synthetic pathways, starting from $F_3S{\equiv}NXeF^+$, have been shown to lead to the $F_4S{=}NXe^+$ cation, namely, solvolysis of $[F_3S{\equiv}NXeF][AsF_6]$ in aHF and solid-state rearrangement of $[F_3S{\equiv}NXeF][AsF_6]$ at ambient temperatures. Structural characterization of the $F_4S{=}NXe^+$ cation has revealed a rare example of xenon bonded to sp^2-hybridized nitrogen, providing the first example of the $F_4S{=}N$-group bonded to a noble gas. The $F_4S{=}NH_2^+$ cation was also formed in the course of HF solvolysis of $F_3S{\equiv}NXeF^+$. The $F_4S{=}NXe^+$ and $F_4S{=}NH_2^+$ cations significantly expand the chemistry of species containing the $F_4S{=}N$-group and represent the only known examples of cations containing this group. The calculated Xe—N bond order of $F_4S{=}NXe^+$ derived from the NBO analyses is consistent with the short Xe—N bond length and high shielding of the ^{129}Xe resonance of $F_4S{=}NXe^+$, which places it, along with the sp^3-hybridized nitrogen cations $F_5SN(H)Xe^+$ and $F_5TeN(H)Xe^+$, among the most covalent Xe—N bonds presently known.

Experimental Section

Caution! *Anhydrous HF must be handled using appropriate protective gear with immediate access to proper treatment procedures[51−53] in the event of contact with liquid HF or HF vapor.*

(50) Gillespie, R. J.; Hargittai, I. *The VSEPR Model of Molecular Geometry*; Allyn & Bacon: Toronto, 1991; pp 143−144.
(51) Bertolini, J. C. *J. Emerg. Med.* **1992**, *10*, 163–168.
(52) Peters, D.; Miethchen, R. *J. Fluorine Chem.* **1996**, *79*, 161–165.
(53) Segal, E. B. *Chem. Health Saf.* **2000**, *7*, 18–23.

Apparatus and Materials. All manipulations involving air-sensitive materials were carried out under strictly anhydrous conditions as previously described.[54] Volatile materials were handled on vacuum lines constructed of nickel, stainless steel, and hexafluoropropylene-tetrafluoroethylene copolymer (FEP). Nonvolatile materials were handled in the atmosphere of a drybox. Reaction vessels and Raman and NMR sample tubes were fabricated from $^1/_4$-in. o.d. and 4-mm o.d. FEP tubing, respectively, and outfitted with Kel-F valves. All reaction vessels and sample tubes were rigorously dried under dynamic vacuum prior to passivation with 1 atm of F_2 gas. Literature methods were used to prepare $N{\equiv}SF_3$[55] and $[F_3S{\equiv}NXeF][AsF_6]$[1] and to purify HF[3] (Harshaw Chemical Co.) and BrF_5[56] (Ozark-Mahoning Co.).

The formation of $[F_4S{=}NXe][AsF_6]$ and $[F_4S{=}NH_2][AsF_6]$ in mixtures with other HF solvolysis products and their isolation from HF are detailed in the Results and Discussion section (see Rearrangement of $[F_3S{\equiv}NXeF][AsF_6]$ in aHF) and in this section under NMR Sample Preparation and Crystal Growth.

$[F_4S{=}NXe][AsF_6]$. Samples of $[F_4S{=}NXe][AsF_6]$ were synthesized by solid-state rearrangement of $[F_3S{\equiv}NXeF][AsF_6]$ (eq 2). In a typical synthesis, $[F_3S{\equiv}NXeF][AsF_6]$ (0.1309 g, 0.2959 mmol) was prepared in a $^1/_4$-in. o.d. FEP tube, fitted with a Kel-F valve, as previously described.[1] The sample was then warmed to 22 °C for a total of ca. 70 min for periods not exceeding ca. 45 min, with periodic cooling to −78 °C for ca. 5 min, to minimize decomposition of $[F_4S{=}NXe][AsF_6]$. Over this time period, conversion of solid white $[F_3S{\equiv}NXeF][AsF_6]$ to a uniformly bright yellow solid occurred which was monitored by low-temperature (−160 °C) Raman spectroscopy. The conversion of $[F_3S{\equiv}NXeF][AsF_6]$ into $[F_4S{=}NXe][AsF_6]$ reached a maximum after a total of ca. 70 min of warming, after which time no further rearrangement was detected by Raman spectroscopy. The sample was stored at −78 °C for several weeks with no sign of further reaction or decomposition.

Nuclear Magnetic Resonance Spectroscopy. (a) NMR Sample Preparation. Samples containing $[F_4S{=}NXe][AsF_6]$ and $[F_4S{=}NH_2][AsF_6]$ were typically prepared in 4-mm o.d. FEP tubes fused to lengths of $^1/_4$-in. FEP tubing fitted with Kel-F valves, which contained $[F_3S{\equiv}NXeF][AsF_6]$ (ca. 0.048 g) prepared in situ, as previously described.[1] The samples were connected to an FEP submanifold that was, in turn, connected through a Kel-F valve to a Kel-F vessel containing aHF or to an FEP vessel containing BrF_5 stored over anhydrous KF. The FEP submanifold was connected to a metal vacuum line, and ca. 0.5 mL of aHF or BrF_5 was statically distilled onto $[F_3S{\equiv}NXeF][AsF_6]$ at −196 °C. For samples containing catalytic aHF in BrF_5 solvent, after BrF_5 had been condensed onto the solute, ca. 0.05 mL of aHF was condensed onto the mixture at −196 °C.

Samples containing $[F_4S{=}NXe][AsF_6]$ in $N{\equiv}SF_3$ solvent were prepared by first synthesizing $[F_4S{=}NXe][AsF_6]$ in situ in the FEP NMR tube by solid-state rearrangement of $[F_3S{\equiv}NXeF][AsF_6]$ (vide supra; ca. 0.048 g). The $[F_4S{=}NXe][AsF_6]$ sample was then connected to a FEP submanifold that was, in turn, connected to a stainless steel cylinder containing $N{\equiv}SF_3$. The FEP submanifold/cylinder assembly was connected to a glass vacuum line, and ca. 0.5 mL of $N{\equiv}SF_3$ was statically distilled onto $[F_4S{=}NXe][AsF_6]$ at −196 °C as previously described.[1]

Nuclear magnetic resonance sample tubes were heat-sealed off under dynamic vacuum and stored at −196 °C until NMR spectra could be obtained. Samples were dissolved at −50 °C and warmed to −20 °C just prior to data acquisition, and they remained at or below this temperature while their spectra were recorded. Low-temperature spectra were obtained by insertion of the sealed 4-mm o.d. FEP sample tube into a 5-mm o.d. thin-wall precision glass NMR tube (Wilmad).

(b) NMR Instrumentation and Spectral Acquisitions. Proton, ^{19}F, and ^{129}Xe NMR spectra were recorded unlocked (field drift < 0.1 Hz h^{-1}) on a Bruker DRX-500 spectrometer equipped with an 11.744-T cryomagnet. The NMR probe was cooled using a nitrogen flow and variable-temperature controller (BV-T 3000).

The ^{19}F (^1H) NMR spectra were acquired using a 5-mm combination $^1H/^{19}F$ probe operating at 470.592 (500.138) MHz. The spectra were recorded in 32K memories, with spectral width settings of 24 (6.8) kHz and acquisition times of 1.39 (2.42) s, and were zero-filled to 64K, yielding data point resolutions of 0.36 (0.21) Hz/data point. Relaxation delays of 0.10 (2.5) s were applied, and 1600 (8) transients were accumulated.

The ^{129}Xe NMR spectra were obtained using a 5-mm broadband inverse probe operating at 138.086 MHz. The spectra were recorded in 32K memories, with spectral width settings of 97.1 kHz and acquisition times of 0.17 s, and were zero-filled to 64K, yielding data point resolutions of 2.96 Hz/data point. Relaxation delays of 0.10 s were applied, and 32 000 transients were accumulated.

Pulse widths, corresponding to tip angles of approximately 90°, were 2.0 (^1H), 8.5 (^{19}F), and 10.0 (^{129}Xe) μs. Line broadenings of 0 (^1H), 0.10 (^{19}F), and 5.0 (^{129}Xe) Hz were used in the exponential multiplication of the free induction decays prior to Fourier transformation. In the case of the ^{19}F NMR spectra of $F_4S{=}NH_2^+$ and $F_4S{=}NXe^+$, Gaussian multiplication was used to enhance spectral resolution.

The ^1H, ^{19}F, and ^{129}Xe spectra were referenced externally at 30 °C to samples of neat $(CH_3)_4Si$, $CFCl_3$, and $XeOF_4$, respectively. The chemical shift convention used is that a positive (negative) sign indicates a chemical shift to high (low) frequency of the reference compound.

(c) Simulation of NMR Spectra. The ^{19}F and ^{129}Xe spectra of the $F_4S{=}NXe^+$ and $F_4S{=}NH_2^+$ cations (AsF_6^- salts in HF at −20 °C) were simulated on a PC using the program ISOTOPOMER.[35] The program provides a full heteronuclear simulation that takes into account natural abundances and second-order effects. Spectra in the present study were not iterated.

Crystal Growth. (a) $[F_4S{=}NXe][AsF_6]$. Anhydrous HF (ca. 1 mL) was condensed at −196 °C onto $[F_4S{=}NXe][AsF_6]$ (0.0889 g, 0.2010 mmol), synthesized in situ by solid-state rearrangement of $[F_3S{\equiv}NXeF][AsF_6]$ (vide supra), in one arm of a $^1/_4$-in. o.d. FEP T-shaped reaction vessel fitted with a Kel-F valve. The reactor was warmed to −40 °C to effect dissolution, giving a yellow solution. While the reaction vessel was maintained at −40 °C, it was attached to a vacuum line, and the arm containing the solution was inclined at ca. 5° from horizontal inside the glass Dewar of a crystal growing apparatus[45] that had been previously adjusted to −40 °C in a nitrogen cold stream. The temperature was lowered over a 15 min period to −50 °C, and yellow needle-shaped crystals began to grow, but with accompanying gas evolution indicative of decomposition. Over the subsequent 15 min period, the temperature was lowered to −67 °C, whereupon gas evolution ceased and more complete crystallization occurred. Crystals were isolated after 30 min at −67 °C by decanting the solvent under dry nitrogen into the side arm of the FEP vessel which was immersed in liquid nitrogen, followed by evacuation and drying of the crystalline product under dynamic vacuum at −70 °C before the side arm containing the supernatant was heat-sealed off. A transparent yellow needle, having the dimensions $0.18 \times 0.06 \times 0.02$ mm^3, was selected at −104 ±2 °C for low-temperature X-ray structure determination and was mounted in a cold stream (−173 °C) on a goniometer head as previously described.[57]

(b) $[F_4S{=}NH_2][AsF_6]$. Anhydrous HF (ca. 1 mL) was condensed at −196 °C onto $[F_3S{\equiv}NXeF][AsF_6]$ (0.1186 g, 0.2681 mmol) that had been synthesized in situ in one arm of a $^1/_4$-in. o.d. FEP T-shaped reactor fitted with a Kel-F valve.[1] The reactor was warmed to −20 °C to effect dissolution and reaction, giving a colorless

(54) Casteel, W. J., Jr.; Dixon, D. A.; Mercier, H. P. A.; Schrobilgen, G. J. *Inorg. Chem.* **1996**, *35*, 4310–4322.
(55) Mews, R.; Keller, K.; Glemser, O. *Inorg. Synth.* **1986**, *24*, 12–17.
(56) Mercier, H. P. A.; Sanders, J. C. P.; Schrobilgen, G. J.; Tsai, S. S. *Inorg. Chem.* **1993**, *32*, 386–393.
(57) Gerken, M.; Dixon, D. A.; Schrobilgen, G. J. *Inorg. Chem.* **2000**, *39*, 4244–4255.

solution. The reaction was allowed to proceed for ca. 30 min at −20 °C, over which time the white solid dissolved, yielding a transparent yellow solution. During this time, the reaction tube was attached to a vacuum line while the reactor was maintained at −20 °C, and the arm containing the solution was inclined at ca. 5° from horizontal inside the glass Dewar of a crystal growing apparatus[45] that had been previously adjusted to −20 °C in a nitrogen cold stream. After 30 min, the temperature was lowered over a period of 5 min to −60 °C, whereupon crystals of several solvolysis products grew. The sample was maintained at −60 °C for a further 10 min to allow for more complete crystallization. Transparent colorless and yellow crystals having four discernible morphologies were isolated by decanting the solvent under dry nitrogen into the side arm of the FEP vessel which was immersed in liquid nitrogen, followed by evacuation and drying of the crystalline materials under dynamic vacuum at −80 °C prior to the heat-sealing of the side arm containing the supernatant. Colorless needles, transparent yellow plates, and colorless plates were present which were identified by unit cell determinations as $[F_3S{\equiv}NXeF][AsF_6]$,[1] $[F_5SN(H)Xe][AsF_6]$,[6] and $[F_5SNH_3][AsF_6]$,[6] respectively. In addition, colorless blades of $[F_4S{=}NH_2][AsF_6]$ were present, and one crystal, having the dimensions 0.24 × 0.10 × 0.06 mm^3, was selected at −104 ±2 °C for a low-temperature X-ray structure determination and was mounted in a cold stream (−173 °C) on a goniometer head as previously described.[57]

X-ray Crystallography. (a) Collection and Reduction of X-ray Data. A crystal of $[F_4S{=}NXe][AsF_6]$ was centered on a Bruker SMART APEX II diffractometer, equipped with an APEX II 4K CCD area detector and a three-axis goniometer, controlled by the APEX2 Graphical User Interface (GUI) software,[58] and a sealed source emitting graphite-monochromated Mo Kα radiation ($\lambda = 0.71073$ Å). Diffraction data collection (at −173 °C) consisted of a full φ-rotation at a fixed $\chi = 54.74°$ with 0.36° (1010) frames, followed by a series of short (250 frames) ω scans at various φ settings to fill the gaps. The crystal-to-detector distance was 49.582 mm, and the data collection was carried out in a 512 × 512 pixel mode using 2 × 2 pixel binning. Processing of the raw data was completed by using the APEX2 GUI software,[58] which applied Lorentz and polarization corrections to three-dimensionally integrated diffraction spots.

A $[F_4S{=}NH_2][AsF_6]$ crystal was centered on a P4 Siemens diffractometer, equipped with a Siemens SMART 1K charge-coupled device (CCD) area detector that used the program SMART,[59] and a rotating anode using graphite-monochromated Mo Kα radiation ($\lambda =$ 0.71073 Å). The diffraction data collection consisted of a full ψ rotation at $\chi = 0°$ using (1040 + 40) 0.36° frames, followed by a series of short (80 frames) ω scans at various ψ and χ settings to fill the gaps. The crystal-to-detector distance was 50.16 mm, and the data collection was carried out in a 512 × 512 pixel mode using 2 × 2 pixel binning. Processing was carried out by using the program SAINT,[59] which applied Lorentz and polarization corrections to three-dimensionally integrated diffraction spots.

For both crystal structures, the program SADABS[60] was used for the scaling of diffraction data, the application of a decay correction, and an empirical absorption correction based on redundant reflections.

(b) Solution and Refinement of the Structures. The XPREP program was used to confirm the unit cell dimensions and the crystal lattices. The final refinements were obtained by introducing anisotropic parameters for all the atoms, an extinction parameter, and the recommended weight factor. The maximum electron densities in the final difference Fourier maps were located around the heavy atoms. All calculations were performed with the SHELXTL-plus package for structure determination, refinement, and molecular graphics.[61] Structure solutions were obtained by direct methods which located the Xe and/or As atoms. Successive difference Fourier syntheses revealed the positions of the fluorine, nitrogen, and sulfur atoms. The positions of the hydrogen atoms in the $F_4S{=}NH_2^+$ cation were calculated (d(N−H) ≈ 1.013 Å; d(H−H) ≈ 1.772 Å; U(H) fixed to $-1.2U$(N)) and were then refined using DFIX restraints.

Raman Spectroscopy. The low-temperature Raman spectrum of $[F_4S{=}NXe][AsF_6]$ (−150 °C) was recorded on a Bruker RFS 100 FT Raman spectrometer using 1064-nm excitation and a resolution of 1 cm^{-1} as previously described.[57] The spectrum was recorded using a laser power of 300 mW and a total of 1200 scans for acquisition of the spectra.

Computational Methods. Quantum-chemical calculations were carried out using B3LYP, PBE1PBE, and MP2 methods as implemented in the Gaussian 03 program[62] for geometry optimizations and vibrational frequencies and intensities for the $F_4S{=}NH_2^+$ and $F_4S{=}NXe^+$ cations and the $[F_4S{=}NXe][AsF_6]$ ion pair. The aug-cc-pVTZ[63] basis sets, as implemented in the Gaussian program, were utilized for all elements except As and Xe, for which the semirelativistic small-core pseudopotential basis sets, aug-cc-pVTZ-PP, were used. The combined use of aug-cc-pVTZ and aug-cc-pVTZ-PP basis sets is indicated as aug-cc-pVTZ(-PP). The program GaussView[64] was used to visualize the vibrational displacements that form the basis of the vibrational mode descriptions given in Tables 4, S3, S4, and S6.

Acknowledgment. This work is dedicated to the memory of Prof. Neil Bartlett (1932−2008), the discoverer of noble-gas reactivity. We thank the Natural Sciences and Engineering Research Council (NSERC) of Canada for financial support in the form of a Discovery Grant (G.J.S.), the Ontario Ministry of Training, Colleges and Universities and the McMaster University Centennial Scholarship Fund for the award of graduate scholarships (G.L.S.), and SHARCNet (Shared Hierarchical Academic Research Computing Network; www.sharcnet.ca) for computational resources. We also thank Dr. J. C. P. Sanders and N. T. Arner for their preliminary NMR work.

Supporting Information Available: Experimental and calculated geometries for the $[F_4S{=}NXe][AsF_6]$ ion pair (Table S1); experimental geometries for the two crystallographically independent AsF_6^- anions in $[F_4S{=}NH_2][AsF_6]$ (Table S2); Raman and calculated vibrational frequencies, intensities, and assignments, geometric parameters, and NBO analyses for $F_4S{=}NF$ (Table S3); experimental and calculated vibrational frequencies, intensities, and assignments for the $[F_4S{=}NXe][AsF_6]$ ion pair (Table S4); correlation diagrams for the vibrational modes of $[F_4S{=}NXe][AsF_6]$ (Table S5); calculated vibrational frequencies, intensities, and assignments for $F_4S{=}NH_2^+$ (Table S6); NBO charges, valencies, and bond orders for $F_4S{=}NXe^+$ and $F_4S{=}NH_2^+$ (Table S7); NBO charges, valencies, and bond orders for $F_5SN(H)Xe^+$ and $F_5TeN(H)Xe^+$ (Table S8); X-ray crystal structure of $[F_4S{=}NXe][AsF_6]$ showing the closest contacts to xenon (Figure S1); complete ref 62; and X-ray crystallographic files in CIF format for the structure determinations of $[F_4S{=}NXe][AsF_6]$ and $[F_4S{=}NH_2][AsF_6]$. This material is available free of charge via the Internet at http://pubs.acs.org.

JA901187N

(58) *APEX2*, release 2.0-2; Bruker AXS Inc.: Madison, WI, 2005.
(59) *SMART*, release 5.054, and *SAINT*, release 056.001; Siemens Energy and Automation Inc.; Madison, WI, 1999.
(60) Sheldrick, G. M. *SADABS (Siemens Area Detector Absorption Corrections)*, version 2.10; Siemens Analytical X-ray Instruments, Inc.: Madison, WI, 2004.
(61) Sheldrick, G. M. *SHELXTL-Plus*, release 6.14; Siemens Analytical X-ray Instruments, Inc.: Madison, WI, 2000−2003.
(62) Frisch, M. J.; et al. *Gaussian 98*, Revision A.11; Gaussian, Inc.: Pittsburgh, PA, 2003.
(63) Dunning, T. H., Jr. *J. Chem. Phys.* **1989**, *90*, 1007–1023.
(64) *GaussView*, release 3.0; Gaussian Inc.: Pittsburgh, PA, 2003.